ASSESSMENT OF LIDAR AND SPECTRAL TECHNIQUES FOR HIGH-RESOLUTION MAPPING OF PERMAFROST ON THE YUKON-KUSKOKWIM DELTA, ALASKA

By

Matthew Allen Whitley, B.S.

A Thesis Submitted in Partial Fulfillment of the Requirements
for the Degree of

Master of Science
in
Geoscience

University of Alaska Fairbanks
May 2017

APPROVED:

Christopher V. Maio, Committee Chair
Gerald V. Frost, Committee Member
M. Torre Jorgenson, Committee Member
Paul McCarthy, Chair
Department of Geosciences
Paul Layer, Dean
College of Natural Science and Mathematics
Michael Castellini, *Dean of the Graduate School*

Abstract

The Yukon-Kuskokwim Delta (YKD) is one of the largest and most ecologically productive coastal wetland regions in the pan-Arctic. Formed by the Yukon and Kuskokwim Rivers flowing into the Bering Sea, nearly 130,000 square kilometers of delta support 23,000 Alaskan Natives living subsistence lifestyles. Permafrost on the outer delta commonly occurs on the abandoned floodplain deposits. Ground ice in the soil raises surface elevations on the order of 1-2 meters, creating plateaus on the landscape. Better drainage on the plateaus supports distinct *Sphagnum*-rich vegetation, which in turn protects the permafrost from rising air temperatures with low thermal conductivity during the summer. This ecosystem-protected permafrost is thus vulnerable to disturbances from rising air temperatures, vegetation mortality, and inland storm surges, which have been known to flood up to 37 km inland.

This thesis assesses several novel techniques to map permafrost distribution at high-resolution on the YKD. Accurate baseline maps of permafrost extent are critical for a variety of applications, including long-term monitoring. As air and ground temperatures rise across the Arctic, monitoring landscape change is important for understanding permafrost degradation processes (e.g. thermokarst) and greenhouse gas dynamics from the local to global scales.

This thesis separately explored the value of Light Detection And Ranging (LiDAR) and spectral datasets as tools to map permafrost at a high spatial resolution. Furthermore, this thesis sought to automate these processes, with the vision of high-resolution mapping over large spatial extents. Fieldwork was conducted in July 2016 to both parameterize and then validate the mapping efforts. The LiDAR mapping extent assessed a 135 km^2 area (~15% permafrost cover), and the spectral mapping extent assessed an 8 km^2 area (~20% permafrost cover). For the LiDAR dataset, the use of a simple elevation threshold informed by field ground truth values provided a permafrost map with 94.9% accuracy. This simple approach was possible because of the extremely flat terrain. For the spectral datasets, an ad-hoc masking technique was developed using a combination of texture analysis, principal component analysis, and morphological filtering. Two contrasting workflows were evaluated with fully-automated and semi-automated methods with mixed results. The highest mapping accuracy was 89.4% and the lowest was 79.1%, though the error of omission in mapping the permafrost remained high (7.02 - 59.7%) for most analyses. The spectral mapping algorithms did not replicate well across different high-

resolution images, raising questions about the viability of using spectral methods alone to track thermokarst and landscape change over time. However, incorporating the spectral methods explored in this analysis with other datasets (e.g. LiDAR) has the potential to increase mapping accuracies. Both the methods and the results of this thesis enhance permafrost mapping efforts on the YKD, and provide a good first step to monitoring landscape change in the region.

Table of Contents

Page

Title Page i

Abstract iii

Table of Contents v

List of Figures vii

List of Tables xi

List of Equations xiii

Acknowledgements xv

1. INTRODUCTION 1

1.1 Study Area 3

2. METHODS 11

2.1 Area of Interest 11

2.2 Fieldwork 12

2.3 LiDAR Mapping 14

2.4 Spectral Mapping 15

2.4.1 Masks 20

2.4.2 Workflow 1 22

2.4.3 Workflow 2 24

2.4.4 Threshold Selection 26

2.4.5 Morphological Filtering 26

2.5 Validation 27

2.6 Comparison Over Time 29

3. RESULTS 31

3.1 Transect Profiles 31

3.2 LiDAR Mapping 38

3.3 Spectral Mapping 46

3.4 Comparison Over Time 52

4. DISCUSSION 55

4.1 Landscape Characteristics 55

4.2 LiDAR Mapping 60
4.3 Spectral Mapping 61
4.3.1 Validation 61
4.3.2 Ad-hoc Masking Technique 64
4.3.3 Spatial and Temporal Landscape Heterogeneity 67
4.4 Viability 68
4.4.1 LiDAR Mapping 68
4.4.2 Spectral Mapping 70
4.5 Broader Impacts 71
5. CONCLUSION 73
6. **LITERATURE CITED** 75

List of Figures

Figure 1. Study Area located on the Yukon-Kuskokwim Delta (YKD) in western Alaska, USA. Depicted in the inset are the spectral mapping Area of Interest (AOI) (cross-hatch), the extent of the 2009 LiDAR data (dashed line), and the approximate distribution of the Lowland Moist Graminoid Shrub Meadow (LMGSM) ecotype (green) (associated with permafrost plateaus) identified by Jorgenson and Roth (2010). 5

Figure 2. Inland gradient map adapted from Jorgenson and Ely (2001) showing examples of relative location, landscape, and soil characteristics for the (A) mudflat, (B) active floodplain, (C) inactive floodplain, and (D) abandoned floodplain. The 2007 IKONOS scene has a false-color infrared NIR-R-G (4-3-2) band combination. Satellite imagery © 2017 Digital Globe, NextView license. 7

Figure 3. Space-time diagram illustrating the hierarchical organization of ecosystems at multiple spatial scales. The terms for each scale of ecological land classification are underlined and the differentiating criteria for each scale are listed. (From Jorgenson 2000) 9

Figure 4. Conceptual model of a permafrost plateau on the YKD. General plateau morphology, vegetation, relative elevation, relative permafrost thickness, and thermokarst processes are illustrated in relation to seaward (left) and landward (right) directions. Morphology of the plateaus can be seen by a steep transition from the coastal meadow to the permafrost plateau on the seaward margin, and a more gradual, sloping transition between ecotypes on the landward margin. This difference in morphology is mirrored in the permafrost thickness under the margins, as well as the species composition and vegetation structure. Vegetation indicative of the LMGSM ecotype on the plateau is represented in this figure with key species (e.g. *Betula nana*, *Rubus chamaemorus*, *Cladina Rangiferina*, etc.), however, for the sake of clarity, not every species is represented. Similarly, the vegetation of coastal meadow ecotypes adjacent to permafrost plateaus is represented with general sedge and grass species. Note the thick organic accumulations in the active layer on the permafrost plateaus that help insulate underlying permafrost from warm summer air temperatures. Indicators of various stages of permafrost degradation are highlighted with grey boxes, and show the main indications of plateau fragmentation. 10

Figure 5. Locations of transects and field validation sampling points in relation to the Tutakoke River, the 2009 LiDAR swath (dashed line), and the spectral mapping AOI (transparent red). The thaw probe transects are shown in red, the field validation points used for the spectral analysis are shown in black, and the field validation points used for the LiDAR analysis are shown in blue. 13

Figure 6. Imagery used in the spectral analysis shown in a false-color infrared NIR-R-G (USFWS: 1-2-3, QB02: 4-3-2, IKONOS: 4-3-2, WV02: 8-5-3) band combination. Satellite imagery © 2017 Digital Globe, NextView license. 17

Figure 7. Flowchart of workflow for LiDAR and spectral mapping. The dashed line shows that the LiDAR derived permafrost map influenced the methods of Workflow 1, but was not directly used in the processing of either workflow until validation. 19

Figure 8. Example of water mask (blue) and shoreline mask (purple) applied in the spectral mapping. The 2007 IKONOS scene is shown in a false-color infrared NIR-R-G (4-3-2) band combination. The insets of blue and purple boxes show detail areas of water and shoreline masks with the LiDAR DEM as backdrop. Satellite imagery © 2017 Digital Globe, NextView license. 21

Figure 9. Base of Workflow 1. Water and shoreline masks are depicted in light purple. The multiplication of the visible bands draws out differences in vegetation type, making the permafrost plateaus appear lighter than the surrounding coastal meadows. The focus of this figure is the base of Workflow 1, not the areas masked out for the analysis. 23

Figure 10. Base of Workflow 2. Water and shoreline masks are depicted in light purple. The second band of the PCA distinguishes between land types, making the permafrost plateaus appear darker than the surrounding coastal meadows. The focus of this figure is the base of Workflow 2, not the areas masked out for the analysis. 25

Figure 11. Thaw Depth (m) by ecotype. Bold horizontal lines show the median thaw depth for each transect, the boxes show the Inter-Quartile Range (IQR)of the thaw data, and the whiskers show 1.5 * IQR ± 1st and 3rd quartiles, respectively. Circles above the whiskers show outliers in the transect as defined by the statistical programming language R (R Development Core Team 2016). Note that the maximum thaw depth was the length of the thaw probe (1.25 m), and indicates lack of permafrost in the majority of cases. 33

Figure 12. Elevation (m above msl) of probing sites along field transects by ecotype. Bold horizontal lines show the median thaw depth for each transect, the boxes show the IQR of the thaw data, and the whiskers show 1.5 * IQR ± 1st and 3rd quartiles, respectively. Circles above and below the whiskers show outliers in the transect as defined by R. 34

Figure 13. Ice wedge found near the southern boundary of the LiDAR swath within the spectral mapping AOI. 37

Figure 14. Result of LiDAR mapping with 2.5 m above msl (mean + 1 standard deviation) threshold. The LMGSM is shown in the background as green, and the 2009 LiDAR extent is shown with a dashed line. The inset enlarges a portion of the spectral mapping AOI to show the result in greater detail 39

Figure 15. Comparison of LiDAR thresholds for mapping permafrost. The 2.5 m above msl (mean + 1 standard deviation) threshold is shown in dark blue, and the 2.3 m above msl (mean) threshold is shown in light blue. Insets enlarge results to see errors of commission highlighted with (i) and (ii) at different points along the LiDAR swath. 41

Figure 16. Probability of near-surface permafrost as predicted by elevation. The logistic regression is shown as a solid black line. The elevation bins are shown with dashed black lines, and the values predicted for each bin from the logistic regression are shown with black circles.

The plus signs show permafrost observations (1 = permafrost, 0 = no permafrost) plotted by their elevation. Presence of permafrost only occurs at the top of the plot (probability = 1), and absence of permafrost only occurs at the bottom of the plot (probability = 0), because of the binomial nature of sampling (i.e. no sites were considered "half permafrost"). The density of permafrost encounters is skewed towards higher elevations, with few observations below 2.1 m above msl, and no observations below 2.0 m above msl. Conversely, the density of samples that did not encounter permafrost were generally found at lower elevations above msl, with few observations above 2.5 m above msl, and no observations above 3.1 m above msl..... 44

Figure 17. Map of the predicted near-surface permafrost probability calculated by 0.1 m elevation bins. High likelihood of near-surface permafrost areas (red) are clearly distinct from low likelihood of near-surface permafrost areas (green), with the areas of uncertainty (yellow) mostly along the margins of the permafrost plateaus. Insets enlarge results to show where previous errors of commission (Figure 15 (i) and (ii)) become distinct by incorporating the logistic regression. 45

Figure 18. Comparative maps of validation based on LiDAR output map: correctly mapped permafrost (blue), correctly mapped non-permafrost (grey), error of omission (red), and error of commission (yellow) is shown for A) Workflow 1, manual threshold selection, B) Workflow 1, automated threshold selection, C) Workflow 2, manual threshold selection, and D) Workflow 2, automated threshold selection. 50

Figure 19. Spectral permafrost mapping error in context of the landscape for A) Workflow 1, manual threshold selection, B) Workflow 1, automated threshold selection, C) Workflow 2, manual threshold selection, and D) Workflow 2, automated threshold selection. Error of omission is shown in red, and error of commission is shown in yellow over the LiDAR data.... 51

Figure 20. Percent of landscape mapped as permafrost (green) and percent error in mapping permafrost (red) for Workflow 1 from 1988-2014. The large variability in the data show the inconsistency of the mapping algorithm across time and sensors. The percent of the landscape mapped as permafrost (y-axis) is close to double true permafrost cover, giving context to the extremely high percent error in mapping permafrost (second y-axis). 52

Figure 21. Percent of landscape mapped as permafrost (green) and percent error in mapping permafrost (red) for Workflow 2 from 1988-2014. The large variability in the data show the inconsistency of the mapping algorithm across time and sensors. The percent of the landscape mapped as permafrost (y-axis) is more realistic than the results of Workflow 1, which is reflected in the percent error in mapping permafrost (second y-axis). Note axis ranges are the same as Figure 20. 53

Figure 22. Schematic of Transect 6, Transect, 8, and Transect 9. Transects have thaw depth (blue), thaw bottom (black), no frost (red), and ground surface (green) lines relative to sea level (grey). Key landscape features are annotated with pictures: A) Low permafrost mounds adjacent to plateaus, B) Wrack line on plateau margin, C) Thermo-erosional gully forming (LWGSM), D) RMGSM ecotype after permafrost plateau subsidence, E) Moderately advanced stage Thermokarst Pit, and F) Permafrost plateau margin. Few field probing sites encountered frost thin enough to break through and determine frost thickness. This figure shows two of these areas

along the margins of permafrost plateaus in Transect 6 (~5 m along transect) and Transect 8 (~70 m along transect). 59

Figure 23. Example of driftwood detection mask, with potential applications for storm surge reconstruction. The 2013 WorldView 02 scene shows the AOI extent in a true-color R-G-B (5-3-2) band combination, and the insets show the 2013 and 2014 WorldView 02 scenes in a false color infrared NIR-Y-G (8-4-3) band combination. Arrows in the insets show differences in driftwood distribution between 2013 and 2014. Satellite imagery © 2017 Digital Globe, NextView license. 66

List of Tables

Table 1. Imagery used for spectral mapping of permafrost. Date, source, nominal spatial resolution (m), and spectral resolution shown. 16

Table 2. Example of logic used for validation, where prime multiplication results in unique values for every outcome. 28

Table 3. Percent permafrost encountered during probing by ecotype. 32

Table 4. Mean elevation (m above msl) by each ecotype probed during fieldwork. 33

Table 5. Descriptive statistics for thaw depths (m) by ecotype. 35

Table 6 Descriptive statistics for elevation (m above msl) by ecotype.. 35

Table 7. LiDAR model accuracy based upon 333 GPS points taken in the field for both the 2.3 m above msl (mean) and 2.5 m above msl (mean + 1 standard deviation) thresholds. The total model accuracy and error is shown in bold. 40

Table 8. Percent error of mapping permafrost in the LiDAR mapping workflow. Errors of omission and commission explain how much of the permafrost on the landscape was missed or added, respectively, in relation to how much permafrost is actually on the landscape. The total percent error is the difference between the percent error of omission and commission. 42

Table 9. Predicted probability of near-surface permafrost calculated for every 0.1 m elevation bin. The table displays the total number of observations that were and were not permafrost in each elevation bin, the total number of observations in each elevation bin (n), and the predicted probability of near surface permafrost calculated from the logistic regression. 43

Table 10. LiDAR model accuracy based upon 333 GPS points taken in the field for a 0.9 probability threshold. The total model accuracy and error are shown in bold. 46

Table 11. Results of spectral mapping validation using GPS points collected in the field. 47

Table 12. Results of spectral mapping validation using LiDAR output map. 47

Table 13. Percent error of mapping permafrost in the spectral mapping workflows, as validated by GPS and LiDAR output map. 48

Table 14. Probability calculated that the spectral mapping workflows are correct given the error in the LiDAR mapping workflow when validating the spectral workflows using the LiDAR output map. 49

Table 15. Percent of the landscape predicted to have permafrost, as calculated from the various validation sets. The LiDAR map was validated using 333 GPS points, of which 71 (21.3%) were permafrost. The spectral maps were validated using both GPS points, and the resultant map of the LiDAR mapping. The validation with GPS used 62 points, of which 45 (75.6%) were permafrost. The validation using the LiDAR output used the entire AOI (17,892,000 pixels) and

found 23.7% and 18.5% permafrost cover with the 2.3 m above msl (mean) and the 2.5 m above msl (mean + 1 standard deviation) thresholds, respectively. 63

List of Equations

Equation 1. Basis of Workflow 1 calculated using the R, G, and B bands of the imagery. 22

Equation 2. Equation for calculating percent error of permafrost mapped..... 28

Equation 3. Probability calculation that the spectral mapping methods were correct in the context of error introduced from the LIDAR mapping method when validating the spectral workflows with the output of the LiDAR Workflow..... 29

Acknowledgements

I would like to acknowledge the following people and organizations that have provided funding and support in some capacity over the course of my thesis. Chief among them would be my committee members: M. Torre Jorgenson, Gerald "JJ" Frost, and Chris Maio; who have constantly provided support and encouragement throughout this lengthy process. Other people I would like to thank include Scott D. Goddard, Samantha G. Winder, and the STAT 654 Consulting seminar for assistance with statistics execution and interpretation. I would also like to thank Matt Macander for his help with data processing and LiDAR adjustment. Ryan Choi and the Welker lab at the remote Tutakoke Camp also provided valuable resources during the field campaign. Finally, I would like to thank Rich Buzard for acting as my partner in crime as a successful graduate student.

Organizations I would like to thank include the National Aeronautic and Space Agency (NASA) Arctic Boreal Vulnerability Experiment (ABoVE) science team (grant #NNH16CP09C), for logistical and institutional support. Being a member of the team is an honor. I would also like to thank the UAF Global Change Student Research Grant award (#G00008751) with funds from the Cooperative Institute for Alaska Research (CIFAR) for their $10,000 award, which greatly facilitated my fieldwork and summer funding. I would like to acknowledge the University of Alaska Fairbanks Graduate School and Thesis Completion Fellowship for funding my final semester. The Alaska Quaternary Center also was a supporter of my research and allowed me to attend the 11th International Conference on Permafrost (ICOP) in June, 2016.

Some companies I would like to acknowledge include Digital Globe, Inc. for the use of their high resolution satellite imagery available through NASA, as well as Esri, HERE, DeLorme, MapmyIndia, OpenStreetMap, and the GIS user community for the Basemaps available in ESRI ArcMap, which are used in many of my images.

1. INTRODUCTION

Permafrost, or perennially frozen ground, is an important landscape feature for much of the Arctic and sub-Arctic regions of the world. An estimated 22-23% of the land cover in the Northern Hemisphere, and 81% of Alaska, is affected by permafrost (Brown et al. 1997, Jorgenson et al. 2008, Cuff and Goudie 2009). As global temperatures rise, landscapes underlain by permafrost are experiencing significant changes, which have far reaching implications for landscape morphology, hydrological processes, ecosystem services, and global carbon cycling (Hinzman et al. 2005, Jorgenson et al. 2010, Romanovsky et al. 2010, Schuur et al. 2015, Liljedahl et al. 2016).

Accurate maps of permafrost distribution and temperature are urgently needed baseline datasets to monitor landscape change. With increasing air and ground temperatures across the Arctic, monitoring permafrost degradation (e.g. thermokarst) is important for understanding processes at both the local and the larger regional and global scales. As roughly 18% of Alaska is considered sporadic permafrost (10-50% landcover) and isolated permafrost (>0-10% landcover) and 31% of Alaska is discontinuous permafrost (50-90%), there is a potentially large area that will be affected by thermokarst and permafrost thaw in the future (Jorgenson et al. 2008). This is especially true on the Yukon-Kuskokwim Delta (YKD), which is near the southern extent of permafrost in Alaska.

Models such as that from Pastick et al. (2015) project declines of 16 to 24% in near-surface permafrost extent by 2100. These projections agree with the projected 22% decrease calculated by Jafarov et al. (2012), which is also comparable to the 20.5 to 24.4% reduction in permafrost extents expected in Canada (Zhang et al. 2008). With even moderate climate projections, such as the Inter-governmental Panel on Climate Change's (IPCC) Representative Concentration Pathway (RCP) 4.5, permafrost is expected to retreat from the present-day discontinuous zone by 2100 (Slater and Lawrence 2013). Extreme climate scenarios, modeled with RCP 8.5, predict that sustainable permafrost will likely only be found in the Canadian Archipelago, Russian Arctic Coast, and east Siberian uplands by 2100 (Slater and Lawrence 2013). With these widespread landscape changes likely on the global scale, having accurate maps of current permafrost extent at the local scale on the YKD is essential. Thus, the main focus of this study is to map permafrost extent on the YKD.

Mapping permafrost landscapes is inherently difficult because permafrost itself is a thermal state, and not a physical terrain (Heginbottom 2002). However, proxies such as vegetation cover, regional air temperatures, topographic anomalies, and characteristic landforms are useful for mapping permafrost cover (Jorgenson and Grosse 2016). Because many permafrost landscapes are remote and logistically challenging to access, the use of remote sensing in permafrost analysis has increased dramatically in recent years (Gogineni et al. 2014, Jorgenson and Grosse 2016). Recent literature reviews provide useful overviews on the current state of permafrost remote sensing techniques (Gogineni et al. 2014, Westermann et al. 2015, Jorgenson and Grosse 2016).

Mapping permafrost extent usually incorporates some sort of process-based model to interpret where permafrost is present or absent. These are diverse in purpose, application, and complexity, but most of them are geophysical in nature and rely on process-based models that determine the thermal state of the ground using heat transfer theory (Riseborough et al. 2008). These methods model surface energy balance between the atmosphere, snow, vegetation, active layer soils, and permafrost. Though generally accurate in determining permafrost presence, these models require many inputs which are hard to model at large spatial scales (e.g. hydrology), or are limited to points associated with boreholes. The Geophysical Institute Permafrost Laboratory (GIPL) model developed by the UAF Geophysical Institute at the University of Alaska Fairbanks is a prime example of a one-dimensional finite-difference numerical model that is spatially constrained to boreholes (Marchenko et al. 2008). Examples of numerical modeling resulting in permafrost extent maps can be found in works by Jafarov et al. (2012) and Slater and Lawrence (2013).

Other models incorporate satellite data, such as one created by Westermann et al. (2015) using MODerate Imaging Spectroradiometer (MODIS) data. Empirical modeling techniques for purposes of mapping permafrost, such as those of Panda et al. (2012), Pastick et al. (2015), and Zhang et al. (2014) tend to use a data fusion approach, combining remote sensing data with field observations, climate models, and thematic maps of a variety of surface and subsurface biophysical characteristics. More physical methods geared to three-dimensional mapping, such as airborne electromagnetic resistivity, have also been conducted (Minsley et al. 2012, Pastick et al. 2013), but have limitations of scale due to their cost.

Due in part to the widespread extent of permafrost around the globe, mapping at several scales is needed to fully understand landscapes in permafrost regions (Riseborough et al. 2008). This study seeks to map permafrost extent at the local scale using high resolution datasets: specifically, Light Detection And Ranging (LiDAR) and high spatial resolution spectral data. Repeat LiDAR has been shown to be useful in tracking thermokarst processes and landscape change in permafrost rich areas (Jones et al. 2013, Paine et al. 2013, Jones et al. 2015, Liljedahl et al. 2016), but to date there has not been an application of LiDAR to map permafrost extent explicitly. High resolution spectral datasets have been previously used to map arctic landscape change related to permafrost, but not on the YKD, and not in a fully automated fashion (e.g. Lin et al. 2012, Tremblay et al. 2012, Lantz et al. 2013, Swanson 2013a, 2013b, Raynolds et al. 2014, Beck et al. 2015, Naito and Cairns 2015). As none of these previous studies focus on the YKD, the lack of a high-resolution baseline dataset hinders analysis of landscape change and the ability to assess the impacts of climate change on permafrost in the region.

In an effort to address this important data gap and explore new mapping techniques, the objectives of the study were to:

1. Collect field data for parameterizing and validating the mapping algorithms;
2. Assess the viability of using LiDAR to map permafrost distribution specifically on the YKD;
3. Assess the viability of using only high-resolution aerial and satellite imagery to map permafrost at the local scale on the YKD; and to
4. Assess the viability of automating these processes in order to observe thermokarst processes from multiple time series.

1.1 Study Area

The YKD of Alaska is one of the largest and most important coastal wetland regions in the Arctic. Located in western Alaska, USA, where the Yukon and Kuskokwim Rivers flow into the Bering Sea, the YKD provides nearly 130,000 km^2 of habitat for migratory geese and waterbirds, making it one of the most biologically productive areas of the arctic tundra biome (Thorsteinson et al. 1989). This productive landscape also helps sustain one of the largest

indigenous human populations in the Arctic. Living in 57 villages, roughly 23,000 Yup'ik and Cup'ik Alaska Natives rely heavily on subsistence lifestyles provided by the delta (Klein 1966, Fienup-Riordan and Rearden 2013). As temperatures and sea levels rise in the Arctic, uncertainty in the stability of coastlines and permafrost may drive landscape change on a region-wide scale, affecting the livelihoods of local communities as well as the habitats of species of conservation concern (Jorgenson and Ely 2001).

This study focuses on the western portion of the YKD south of the village of Chevak and West of Hazen Bay (Figure 1). This region of the YKD is extremely flat, as previous elevation profiles by Jorgenson and Ely (2001) show topographic gradients of as little as 0.5 m over 7.5 km. The lack of topography makes the YKD highly vulnerable to eustatic sea-level rise and inland storm surges, which have been known to flood up to 37 km inland (Terenzi et al. 2014).

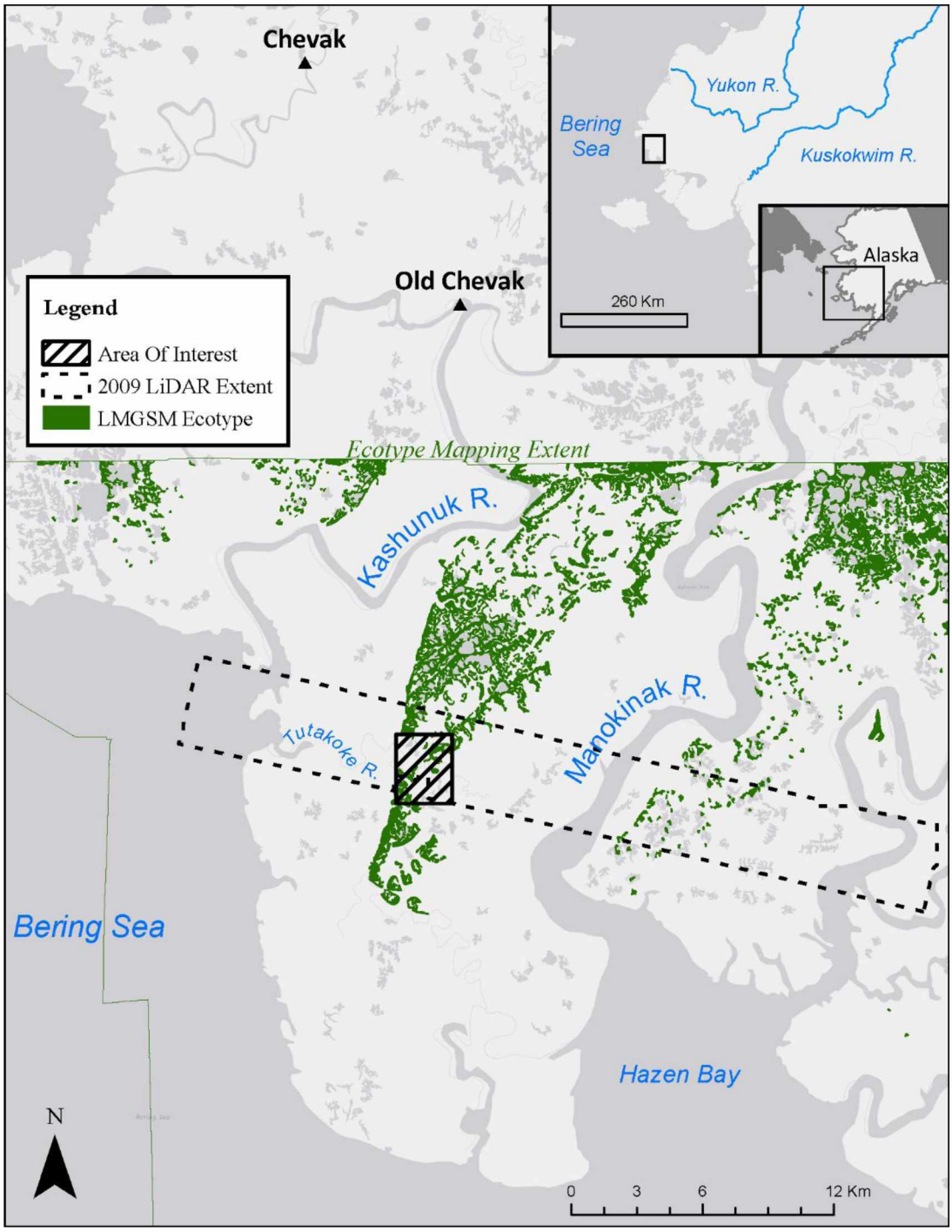

Figure 1. Study Area located on the Yukon-Kuskokwim Delta (YKD) in western Alaska, USA. Depicted in the inset are the spectral mapping Area of Interest (AOI) (cross-hatch), the extent of the 2009 LiDAR data (dashed line), and the approximate distribution of the Lowland Moist Graminoid Shrub Meadow (LMGSM) ecotype (green) (associated with permafrost plateaus) identified by Jorgenson and Roth (2010).

This landscape is quite far south for permafrost extent in Alaska, and lies in the sporadic to isolated permafrost zone (Jorgenson et al. 2008). The Mean Annual Air Temperature (MAAT) in Bethel, AK is -1.2°C (1923-present), making the region very warm for supporting permafrost (Péwé and Brown 1973, NOAA/NCDC 2017). The NOAA/NCDC (2017) data show a warming trend that will likely result in MAATs above 0°C in the future. Under these climatic conditions, the permafrost is considered ecosystem-protected permafrost, meaning that insulative cover of vegetation and organic matter allows the permafrost to remain stable under normally incompatible temperatures (Shur and Jorgenson 2007). Furthermore, ecosystem-protected permafrost is unlikely to re-form after disturbance, so accurately mapping permafrost extent in this region is important to monitoring permafrost resiliency.

The permafrost here is unique in that it only forms on certain parts of the delta, fitting with the geomorphic gradient outlined by Jorgenson (2000) and Jorgenson and Ely (2001). Loosely tied to a gradual elevation ramp from sea level inland, the landscape progresses from coastal mudflats to active floodplains, then to inactive floodplains, and finally to abandoned floodplains farther inland. Permafrost in the area predominantly manifests on the abandoned floodplains, as interactions from storms and tides prohibit permafrost formation closer to the coast (Jorgenson and Ely 2001, Terenzi et al. 2014). This gradient dictates differences in vegetation and soil stratigraphy, as well as the presence or absence of permafrost. The mudflats and active floodplains have the highest rates of sedimentation (8.0 mm/y and 1.4 - 6.5 mm/y, respectively) due to annual flooding, but the least soil organic layer development (Jorgenson and Ely 2001). Inactive floodplains show moderate amounts of sedimentation (0.1-0.2 mm/y) and organic layer formation, and flood every 3-4 years, as interpreted from the stratigraphy of soil plugs (Jorgenson and Ely 2001). The abandoned floodplain rarely sees sedimentation, and has large amounts of organic accumulation in the soil stratigraphy. This thick soil organic layer helps in part to insulate the permafrost, maintaining stable temperatures in the relatively warm climate, and promotes permafrost development in the region. Figure 2 illustrates differences in landscape along the geomorphic gradient.

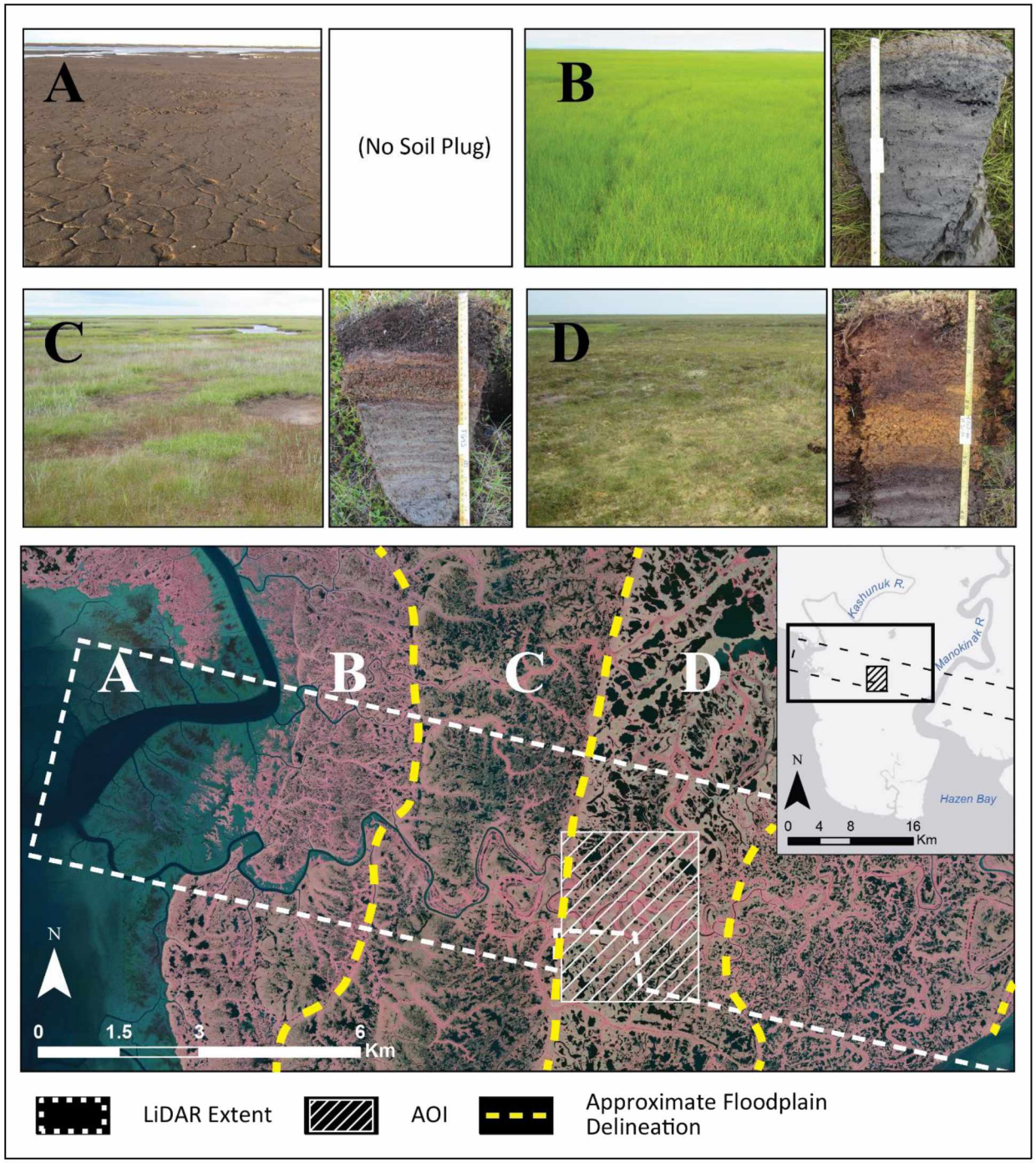

Figure 2. Inland gradient map adapted from Jorgenson and Ely (2001) showing examples of relative location, landscape, and soil characteristics for the (A) mudflat[1], (B) active floodplain, (C) inactive floodplain, and (D) abandoned floodplain. The 2007 IKONOS scene has a false-color infrared NIR-R-G (4-3-2) band combination. Satellite imagery © 2017 Digital Globe, NextView license.

1. No soil plug was taken for the mudflat in the 2016 field season.

Permafrost in the region manifests as plateaus on the landscape because segregated ice in the soil raises the ground surface on the order of 1-2 m (Jorgenson and Ely 2001). Because of the elevation difference, the permafrost plateaus have better drainage and support vegetation that is less tolerant to salt and inundation. Vegetation on the plateaus consists mainly of herbaceous plants such as *Eriophorum angustifolium, E. russeolum, Calamagrostis deschampsioides, Carex rariflora,* and *Rubus Chamaemorus*[2], with low and dwarf shrubs *Betula nana*, Rhododendron subarcticum*, Empetrum nigrum, Salix fuscescens**, as well as mosses (*Sphagnum** spp. and *Dicranum** spp.) and lichens (*Cladonia** spp. and *Cladina** spp.) (Jorgenson and Ely 2001, Jorgenson and Roth 2010). The surrounding lowlands are mostly sedge meadows, which include *Carex aquatilis, C. rariflora, C. lyngbyei, Salex fuscescens, Eriophorum scheuzeri, Potentilla palustris,* and *Empetrum nigrum* (Jorgenson and Ely 2001, Jorgenson and Roth 2010). The permafrost plateaus have a higher heterogeneity in species composition and vegetation structure than the surrounding lowlands, and are generally more diverse. Due to these vegetation characteristics, Jorgenson and Roth (2010) classify the permafrost plateaus as a Lowland Moist Graminoid Shrub Meadow (LMGSM) ecotype, with the surrounding lowlands as a Lowland Moist Sedge Meadow (LMSM) ecotype. Here, *ecotype* refers to the most detailed level of classification for local ecosystems: a 1:1,000-scale unit that has homogeneous topography, soils, hydrology, and vegetation (Figure 3) (Jorgenson 2000, Jorgenson and Ely 2001). Differences in the cover of plant functional type between the plateaus and the surrounding meadows contribute largely to the formation of permafrost on the plateaus. The lichen- and moss-rich plateaus have thermal properties conducive to formation and protection of permafrost, where higher thermal conductivity in the winter allows for heat loss from the ground, but low thermal conductivity in the summer insulates underlying permafrost from warmer air temperatures. Figure 4 provides a conceptual model of a permafrost plateau on the YKD, highlighting vegetation, elevation, and morphological differences from the surrounding coastal meadows, as well as indicators of permafrost degradation on the landscape.

2. * Indicate species that are highly intolerant to brackish water interaction from periodic inland storms

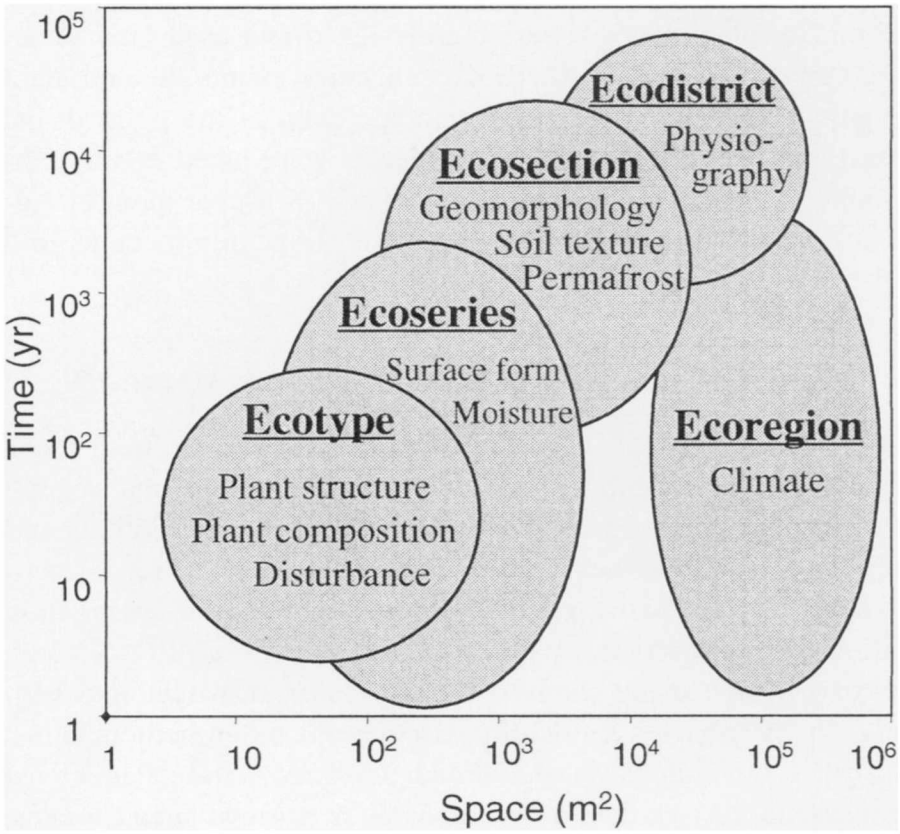

Figure 3. Space-time diagram illustrating the hierarchical organization of ecosystems at multiple spatial scales. The terms for each scale of ecological land classification are underlined and the differentiating criteria for each scale are listed. (From Jorgenson 2000)

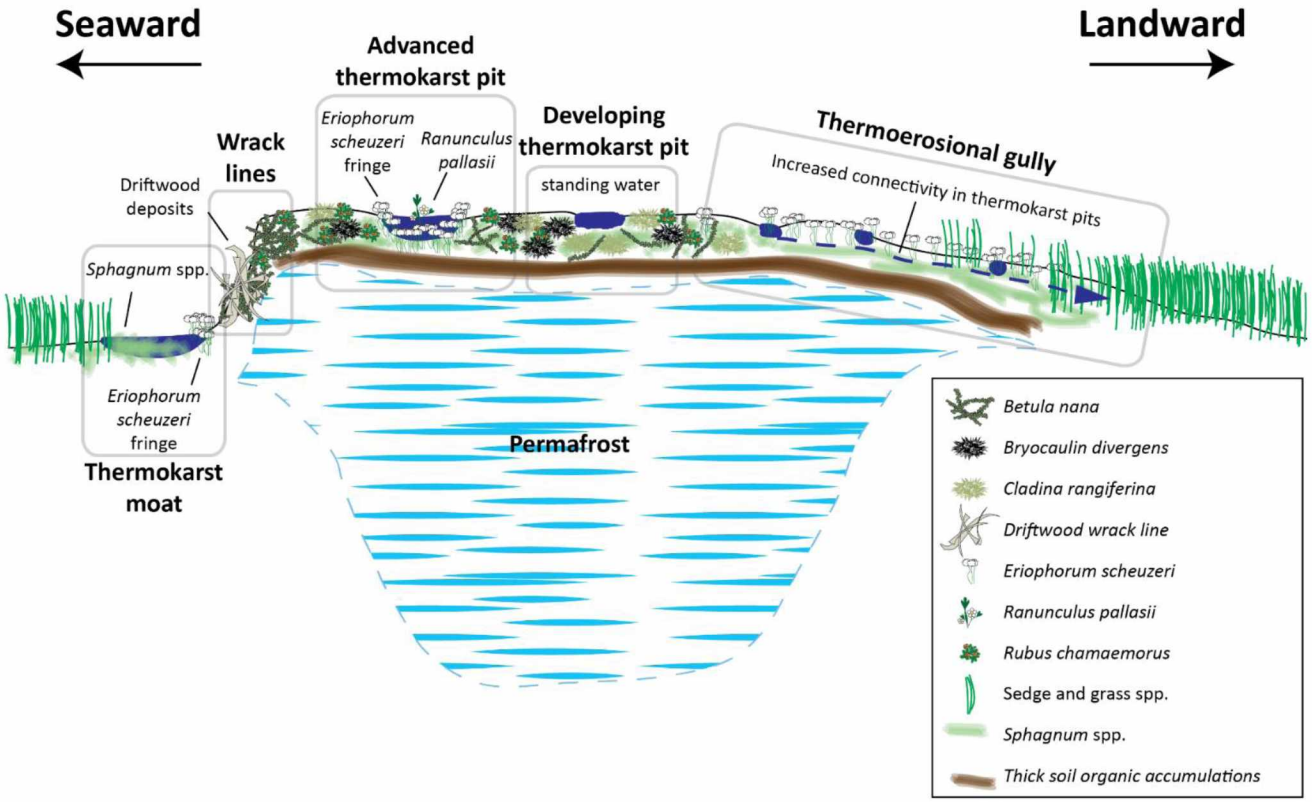

Figure 4. Conceptual model of a permafrost plateau on the YKD. General plateau morphology, vegetation, relative elevation, relative permafrost thickness, and thermokarst processes are illustrated in relation to seaward (left) and landward (right) directions. Morphology of the plateaus can be seen by a steep transition from the coastal meadow to the permafrost plateau on the seaward margin, and a more gradual, sloping transition between ecotypes on the landward margin. This difference in morphology is mirrored in the permafrost thickness under the margins, as well as the species composition and vegetation structure. Vegetation indicative of the LMGSM ecotype on the plateau is represented in this figure with key species (e.g. *Betula nana*, *Rubus chamaemorus*, *Cladina Rangiferina*, etc.), however, for the sake of clarity, not every species is represented. Similarly, the vegetation of coastal meadow ecotypes adjacent to permafrost plateaus is represented with general sedge and grass species. Note the thick organic accumulations in the active layer on the permafrost plateaus that help insulate underlying permafrost from warm summer air temperatures. Indicators of various stages of permafrost degradation are highlighted with grey boxes, and show the main indications of plateau fragmentation.

2. METHODS

To achieve the project objectives, several steps needed to be accomplished. First, a suitable study site on the delta was selected. Second, field work was performed to collect new data for developing and validating mapping algorithms. Third, automated mapping techniques were developed for LiDAR and spectral datasets using predominantly Python scripting in a Linux environment. These analyses relied heavily on the use of the Geospatial Data Abstraction Library (GDAL), and the NumPy and SciPy modules, with occasional use of ENVI version 5.3 and ArcGIS version 10.4 (Jones et al. 2001-, ENVI 2015, ESRI 2015, GDAL 2015). All analyses were performed in the NAD83 Universal Transverse Mercator (UTM) Zone 3 North projection. Mapping results were then validated using a variety of methods, and compared to determine the most viable mapping algorithms.

2.1 Area of Interest

The selected Area of Interest (AOI) covers approximately 8 km^2 of mostly abandoned floodplain roughly 7 km inland from the coast (Figure 1). Because the AOI was based on an aerial single frame collected in 1988, it only partially intersects the 128 km^2 LiDAR swath used in the LiDAR mapping analysis. For this reason, validation of the spectral mapping using the results of the LiDAR mapping were restricted to the northern half of the AOI.

The study site along the Tutakoke River made a good candidate for mapping permafrost, because it had distinct topographical and vegetative characteristics. Because the plateaus only manifest where there is permafrost, the YKD is a unique study site topographically, making high resolution Digital Elevation Models (DEMs) derived from LiDAR a powerful mapping resource. Similarly, the distinct vegetation on the plateaus can serve as a proxy for mapping permafrost extent. These landscape characteristics, in coordination with existing long-term ecological surveys, temporary tide gauges, vegetation monitoring plots, and available satellite and aerial imagery coverage were taken into consideration when selecting an AOI.

2.2 Fieldwork

A field campaign was conducted from July 8 to July 18, 2016 to collect *in situ* data needed for analysis and validation. Transects running perpendicular to the boundary of permafrost plateaus were established subjectively according to the type of vegetation present, presence of storm indicators (e.g. driftwood), evidence of thermokarst (e.g. thermokarst pits, thermokarst moats, thermo-erosional gullies, etc.), and location in the AOI. Each transect was sampled regularly at 5 m intervals where no permafrost was present, at 1 m intervals where permafrost was present, and at intervals <1 m in targeted areas of interest (i.e. driftwood deposits and permafrost transition zones). Thaw depths were measured using a 1.25 m thaw probe and a Delorme PN-60 GPS (positional accuracy greater than 3m). Frost presence or absence was recorded at each probe location along the transect, as well as ecotype and dominant vegetation present. Since sampling was conducted in July, it is likely some of the frost encountered was only seasonal frost, not true permafrost. If seasonal frost was measured, it was most likely encountered along the margins of the plateaus. When possible, the depth to the bottom of the thaw was also measured. This entailed breaking through the frost with the thaw probe and measuring how thick the frost layer was. This was only feasible near the margins of the plateaus, or on highly degraded plateaus. This added effort was important for describing the relative thickness of the permafrost, and also allowed for the discovery of taliks (thaw bulbs). These transects help to describe the boundary conditions between permafrost plateaus and the surrounding lowlands that are, ultimately, of interest for tracking thermokarst of the plateaus.

For validation, 467 GPS points and probe measurements were collected in addition to those collected along the transects. These validation points were later categorized as binary permafrost/not permafrost for use in validating the following mapping techniques. Figure 5 shows locations of transects, the AOI used for spectral mapping, the LiDAR swath, and validation points.

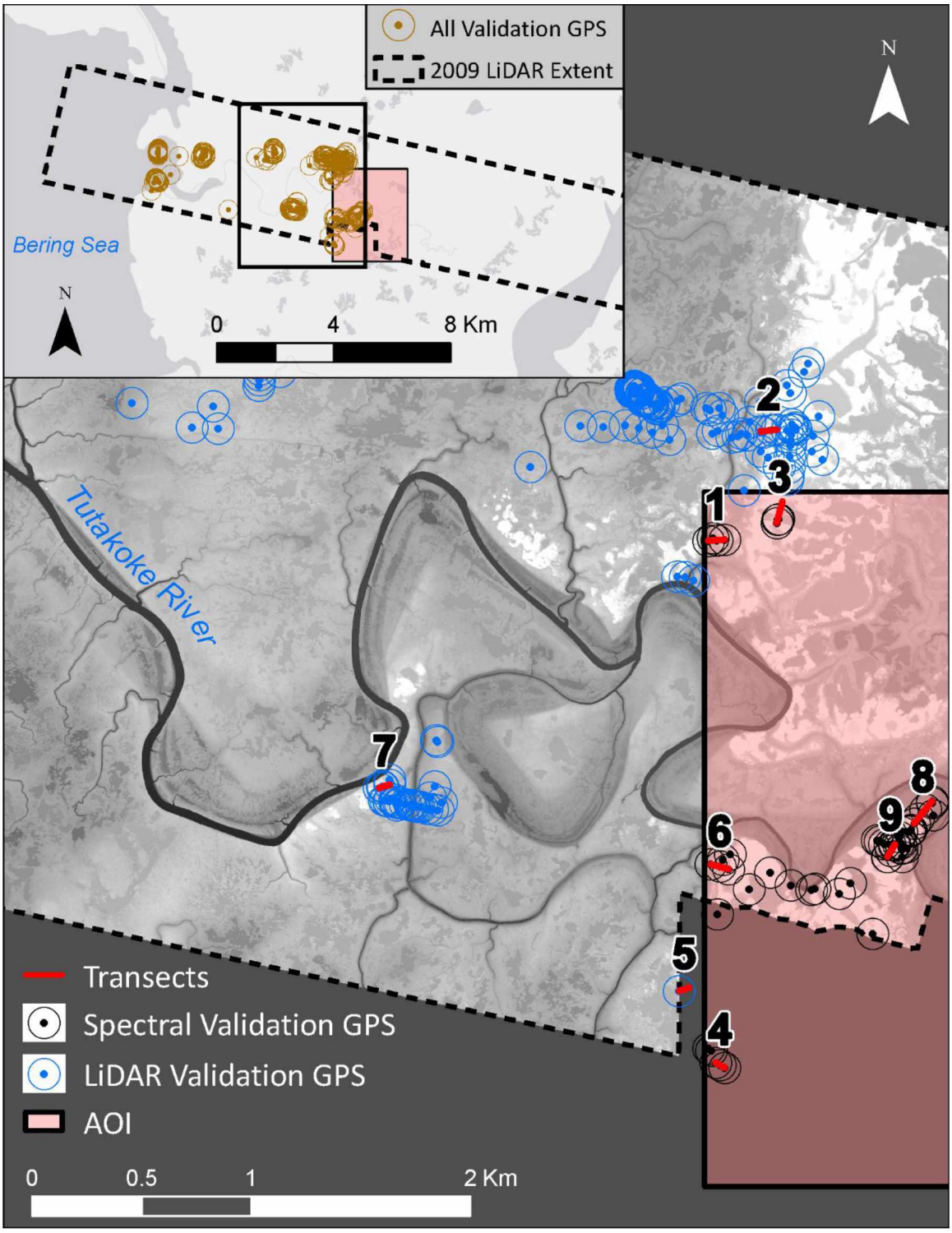

Figure 5. Locations of transects and field validation sampling points in relation to the Tutakoke River, the 2009 LiDAR swath (dashed line), and the spectral mapping AOI (transparent red). The thaw probe transects are shown in red, the field validation points used for the spectral analysis are shown in black, and the field validation points used for the LiDAR analysis are shown in blue.

The transects were then analyzed by ecotype and elevation extracted from the LiDAR DEM. Similar ecotypes were grouped together for purposes of simplification and to ensure a minimum sample size of at least 10 observations per ecotype. The average elevation and the percent permafrost were then calculated for each of the seven ecotypes. Locations probed that encountered frost were also analyzed in the context of ecotype, where pairwise differences between ecotypes were tested for significance with an Analysis of Variance (ANOVA) and a subsequent Dunnett-modified Tukey-Kramer (DTK) test (Dunnett 1980). Elevations above Mean Sea Level (msl) were similarly analyzed by ecotype.

2.3 LiDAR Mapping

Because of the high correlation between permafrost and elevation on the otherwise flat delta, high resolution Digital Elevation Models (DEMs) derived from LiDAR are well suited for mapping permafrost presence or absence in this area. A LiDAR mission flown between 6/27/2009 and 7/2/2009 by Kodiak Mapping Inc. for the U.S. Fish and Wildlife Service was the base dataset used for this mapping (Airborne Imaging 2011). The LiDAR dataset contained few multiple returns (reflectance from the canopy and the ground), and most of the points were only single returns (only reflectance from the ground). For this reason, only last returns were considered when making the DEM. After point density of the LiDAR returns were analyzed and the terrains were built, the terrains were converted to a raster DEM with 1 m horizontal resolution and 0.05 m vertical resolution (Airborne Imaging 2011).

The 2009 LiDAR DEM was subsequently adjusted to elevation above msl with a three step process that 1) determined the mean sea level for the area based on an *in situ* tide gauge, 2) compared the water level with ground control networks from 1997 and 2010, and 3) calculated the offset for the 2009 LiDAR DEM. Msl was calculated from an Onset Hobo Data Logger tide gauge deployed from 7/28/2009 to 11/30/2010. The tide gauge was found to be consistent with most of the ground control available, but was ultimately tied to the 1997 control network for consistency with 15 years of previous analyses and publications (Jorgenson 2000, Jorgenson and Ely 2001). The tide-corrected LiDAR elevations were 0.98 m lower than the NGVD88 vertical datum based on the GEOID96 model in which the LiDAR data were originally processed.

Using the corrected LiDAR dataset, elevations of the edges of the permafrost plateaus were then extracted from the points sampled in the field. This was performed through manual identification of the transitions from permafrost plateau to coastal meadow in a GIS. To map the extent of permafrost in the LiDAR swath, two thresholds were selected based upon the descriptive statistics of the extracted elevation. The first was the relatively conservative threshold of the mean elevation of the permafrost boundaries. The second was the mean elevation of the boundaries plus one standard deviation. These thresholds were then used to create a binary mask of areas with permafrost (elevations above the threshold) and areas without permafrost (elevations below the threshold). With these thresholds, two maps were created from the DEM and validated using the 467 validation points collected in the field (Figure 15).

The relationship between elevation and permafrost occurrence was also analyzed using logistic regression by looking at whether or not permafrost was encountered at each field probe site (not just those on the boundaries of the plateaus). Elevations were extracted from the LiDAR DEM at each probe site and modeled against presence or absence of permafrost at that site. The resulting model was used to predict the probability of permafrost occurrence within 0.1 m elevation bins that spanned all observed elevations. The LiDAR was then grouped into these bins, color-coded by the predicted probabilities, and subsequently mapped. This resulted in a "probability map" that serves to quantify the uncertainty of whether or not permafrost is present in each area.

2.4 Spectral Mapping

The spectral mapping was performed on five high resolution aerial and satellite datasets (Table 1). Each dataset was orthorectified, and radiometrically corrected within the GIS, if possible. The scenes were then co-registered to the 1988 scene, which had the highest resolution and best orthorectification; all scenes had a Root Mean Square Error (RMSE) of <1 m $\pm$ 0.1 m. Finally, each scene was resampled to a 0.5 m grid for consistency using a cubic convolution resampling technique, and clipped to the spectral mapping AOI (Figure 6). The following mapping algorithms were first developed using the 2007 IKONOS scene, and then applied to other datasets for comparison throughout time. Two workflows are presented here for comparison of accuracy and the assessment of automation techniques.

Table 1. Imagery used for spectral mapping of permafrost. Date, source, nominal spatial resolution (m), and spectral resolution shown.

Date	Source	Spatial Resolution (m)	Spectral Resolution
29-Jun-1988	US Fish and Wildlife survey	0.35	NIR, R, G,
17-Jul-2003	QuickBird 02	2.5	R, G ,B, NIR
27-Aug-2007	IKONOS	1	R, G, B, NIR
11-Jul-2013	World View 02	0.5	6 visible bands, 2 NIR
20-Jun-2014	World View 02	0.5	6 visible bands, 2 NIR

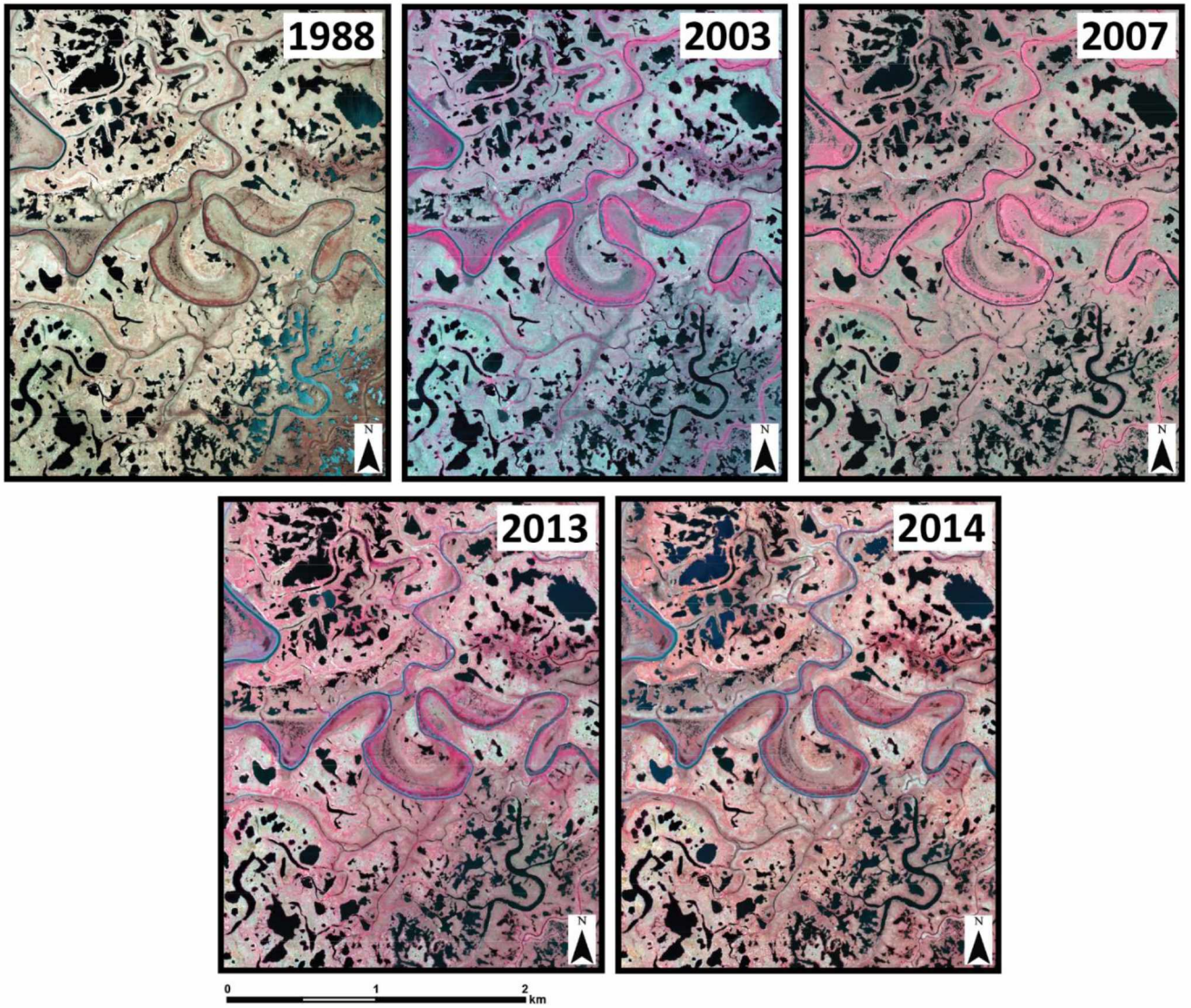

Figure 6. Imagery used in the spectral analysis shown in a false-color infrared NIR-R-G (USFWS: 1-2-3, QB02: 4-3-2, IKONOS: 4-3-2, WV02: 8-5-3) band combination. Satellite imagery © 2017 Digital Globe, NextView license.

To map permafrost extent, an ad-hoc masking technique was developed to identify areas known to lack permafrost and remove them from analysis before spectral thresholds were employed in identifying the plateaus. The two masks utilized in the final analysis identified water features and shorelines between permafrost plateaus and water. The spectral techniques used in identifying these masks and thresholds came from a combination of Principle Component Analysis (PCA), texture analysis via Grey Level Co-occurrence Matrix (GLCM), and morphological filtering (Haralick and Shanmugam 1973, Jolliffe 2002, Soille 2013). A diagram of this workflow is shown in Figure 7.

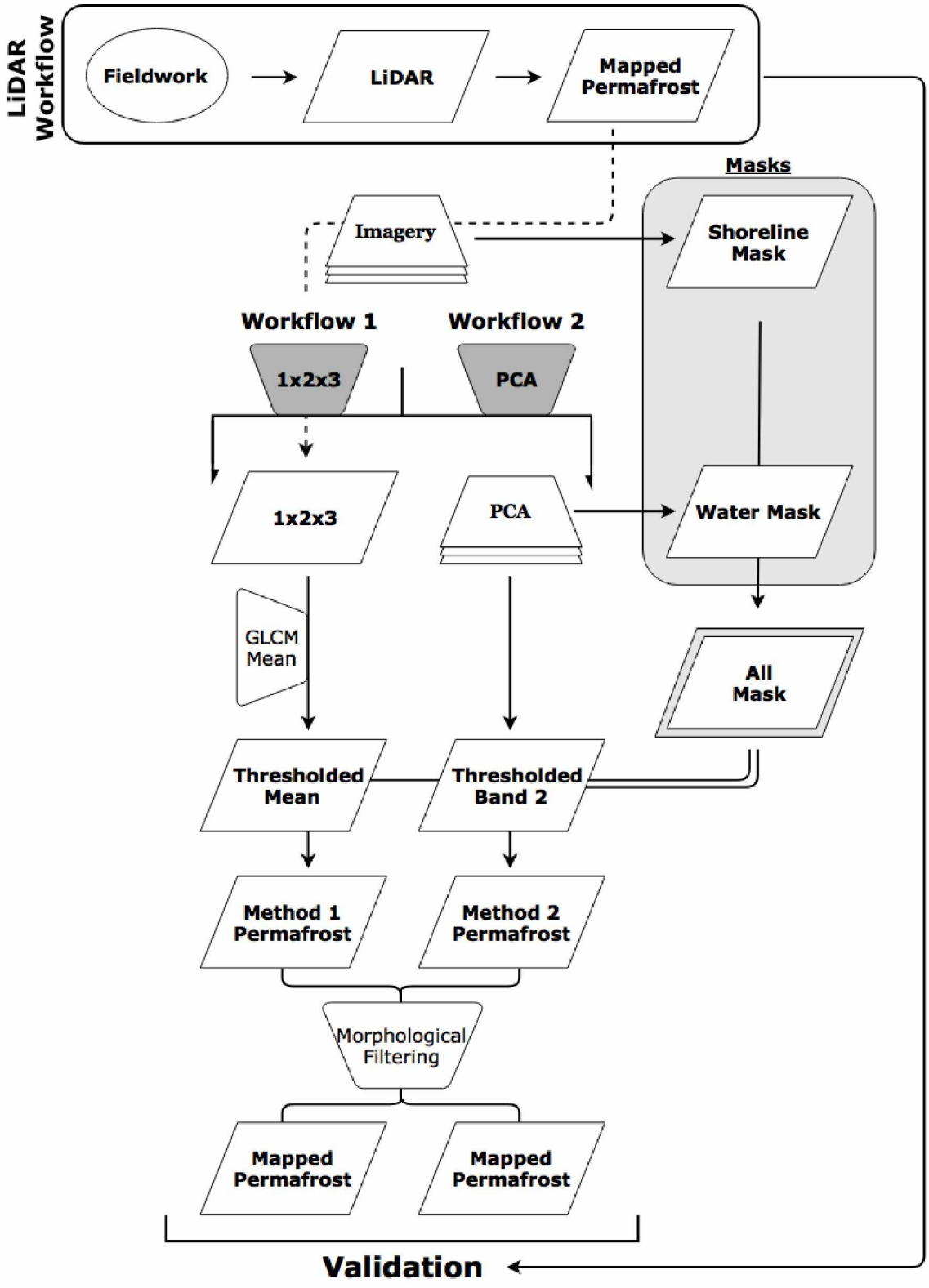

Figure 7. Flowchart of workflow for LiDAR and spectral mapping. The dashed line shows that the LiDAR derived permafrost map influenced the methods of Workflow 1, but was not directly used in the processing of either workflow until validation.

2.4.1 Masks

Two different masks were created in order to exclude areas known not to have permafrost. These landcover types were water bodies, and relatively thin shorelines adjacent to both water bodies and margins of permafrost plateaus.

Since no single band perfectly masked water features, the water mask was made by using the first principal component from a PCA run on the unmodified bands of the image. The first principal component (i.e. the first PCA band) accounted for 93.20% of the variance in the dataset, and showed a clear bimodal distribution of water and land in the histogram of the first PCA band. The mask was automated by thresholding the first PCA band using the Otsu segmentation method available in the scikit-image toolbox of SciPy (Otsu 1979, Walt et al. 2014).

The second mask identified shorelines using statistical texture analysis (Haralick and Shanmugam 1973). Because the water had low reflectance in the Near Infra-Red (NIR) band and the permafrost had relatively high reflectance in the NIR, the statistical variance of a 5x5 kernel convolved with the image accurately captured the lowland transition between permafrost plateaus and water features. Simply taking the data greater than or equal to the mean plus one standard deviation of the image histogram efficiently automated the production of the mask. (Figure 8). These masks were combined to later be used on the separate workflows before final threshold selection and morphological filtering.

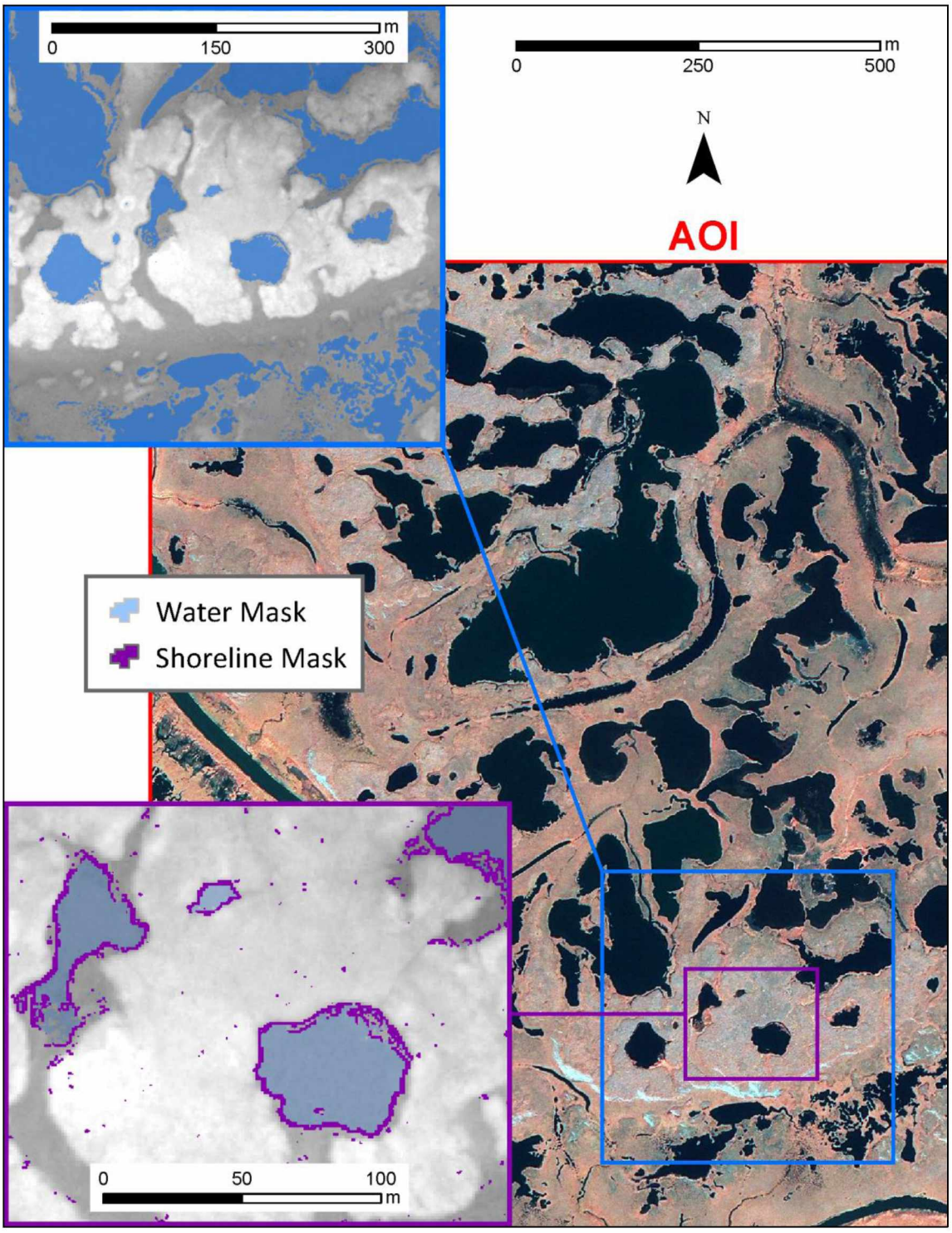

Figure 8. Example of water mask (blue) and shoreline mask (purple) applied in the spectral mapping. The 2007 IKONOS scene is shown in a false-color infrared NIR-R-G (4-3-2) band combination. The insets of blue and purple boxes show detail areas of water and shoreline masks with the LiDAR DEM as backdrop. Satellite imagery © 2017 Digital Globe, NextView license.

2.4.2 Workflow 1

To understand the general spectral differences between the permafrost plateaus and the surrounding coastal meadows, the results from the LiDAR mapping were used to extract a sample of pixels from the plateaus and the meadows. Descriptive statistics found the permafrost plateaus overall had higher reflectances in the red, green, and blue bands than the surrounding coastal meadows, but lower reflectances in the NIR band. Similarly, the meadows were fairly homogeneous floristically and spectrally, whereas the plateaus themselves contained more of a mixed signal due to the heterogeneity of the vegetation on the plateaus. In context, this agrees with the heterogeneity of the vegetation on the plateaus compared to that of the meadows. In an effort to distinguish between permafrost plateau and coastal meadow, this relationship was exploited by multiplying the red, green, and blue bands together to draw the spectral signatures apart (Equation 1). This product served as the basis for Workflow 1.

Equation 1. Basis of Workflow 1 calculated using the R, G, and B bands of the imagery.

$$W^1 = L_r \cdot L_g \cdot L_b$$

Where W^1 = base of Workflow 1,
L_r = radiance of the red band,
L_g = radiance of the green band, and
L_b = radiance of the blue band,

To homogenize the plateaus and reduce speckle gained from multiplication, a 5x5 kernel was convolved with the scene to take the statistical mean of the data. This low-pass filter smoothed the entire scene, and coincidently resulted in the loss of resolution. The plateaus in the resulting raster had higher values (in radiance[3]) than the surrounding lowlands (Figure 9). At this point, the water and shoreline masks were applied and subsequent processing was identical for Workflow 1 and Workflow 2.

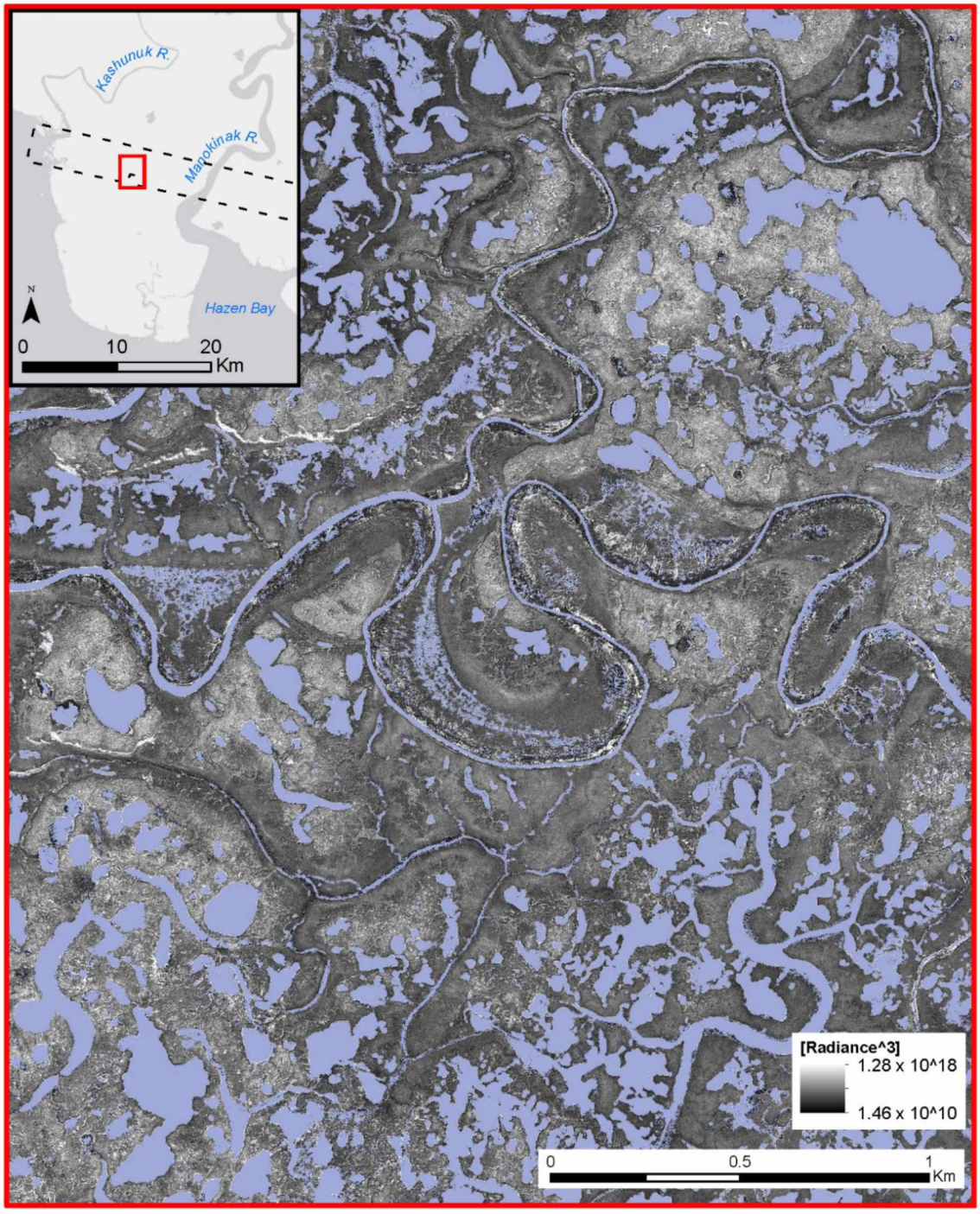

Figure 9. Base of Workflow 1. Water and shoreline masks are depicted in light purple. The multiplication of the visible bands draws out differences in vegetation type, making the permafrost plateaus appear lighter than the surrounding coastal meadows. The focus of this figure is the base of Workflow 1, not the areas masked out for the analysis.

2.4.3 Workflow 2

Workflow 2 is a continuation of the PCA conducted on the unmodified bands, which was used for creating the water mask (2.4.1). Whereas the first principal component accounted for the difference between water and land within the AOI, the second principal component distinguished between different types of land (determined visually). This second principle component band became the base for Workflow 2. The second PCA band accounted for 6.38% of the variation in all the data of the scene. Together, the first two components of the PCA account for 99.58% of the variation within the data, so the remaining components were considered noise. Unlike Workflow 1, the plateaus in the resulting raster had lower values (unit-less) than the surrounding lowlands (Figure 10). Again, the masks were applied to the data, and both workflows continued with the same analysis.

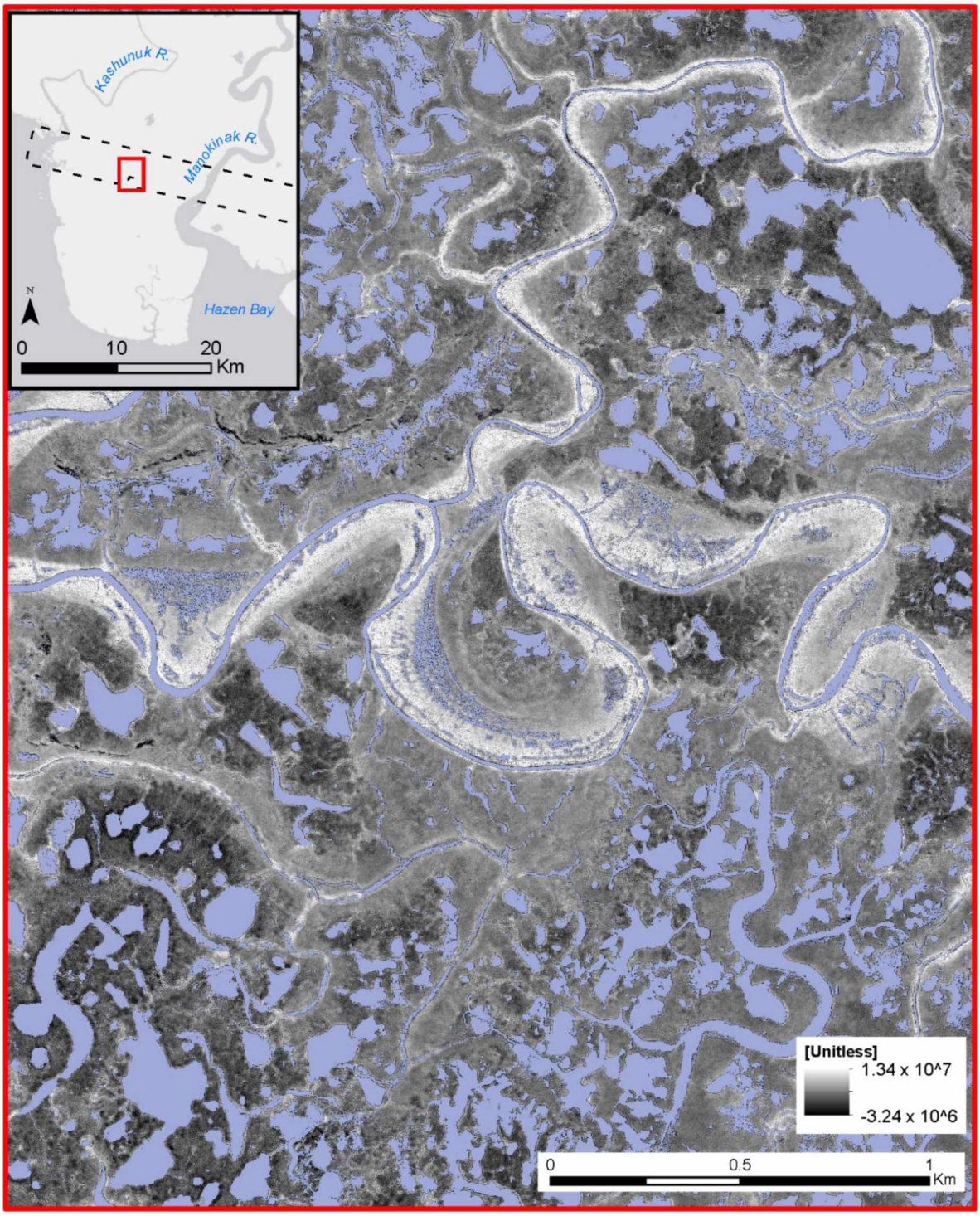

Figure 10. Base of Workflow 2. Water and shoreline masks are depicted in light purple. The second band of the PCA distinguishes between land types, making the permafrost plateaus appear darker than the surrounding coastal meadows. The focus of this figure is the base of Workflow 2, not the areas masked out for the analysis.

2.4.4 *Threshold Selection*

To create a binary image of permafrost and non-permafrost landscapes, a threshold is needed to define the transition between land cover types. Selecting these thresholds was the most difficult part of the analysis to automate. In an effort to create a workflow that was not reliant on manual threshold selection, thresholds for both workflows were determined based upon the histograms of the images. Several automatic thresholds were tested as cutoffs, but the mean digital number (pixel value) of the image efficiently produced results most similar to manual selection.

Thresholds were manually selected to help assess the accuracy of an automated threshold selection process. Thresholds were selected for each workflow based upon visual interpretation of the plateaus in the scene. The subjective nature of this task introduced some uncertainties, and is likely difficult to reproduce accurately. The substantially larger amount of time and effort needed for the manual threshold selection was also considered in determining the workflow of the final mapping algorithm. Once thresholds were selected, both workflows were converted to binary rasters (i.e. permafrost/non-permafrost) in order to perform morphological filtering.

2.4.5 *Morphological Filtering*

Morphological filtering is a series of non-linear operations applied to an image that manipulate its size and shape (Soille 2013). A series of morphological filters were applied to the datasets in an effort to clean up noise and remove stray pixels, similar to a clumping and sieving operation. In particular, the Morphological Opening operation was applied. This operation first eroded the edges of the identified permafrost pixels for a number of iterations (making the shapes smaller), then dilated the remaining groups for the same number of iterations (making the shapes larger again). This process removed small clusters of pixels that disappeared during the erosion process, but left larger plateau groups, returning them to their original size and general shape with the dilation.

Two different structuring elements were used to perform two sets of iterations of the morphological filtering. A structuring unit's size dictates how severe the morphological operation will be, so different units were used for different purposes. The first morphological unit was a 3x3 kernel with a cross structure that was iterated twice. This structure was more severe in removing noise from the images. The second structure was a 2x2 square that was

iterated 8 times. This structure was less severe, and performed better in maintaining the shapes of the plateaus. Both were implemented in an effort to balance accurate representation of the plateaus with removing as much noise from the scenes as possible. Finally, both masks were once again applied to rid the final selection of any erroneous permafrost detection due to the morphological filtering.

2.5 Validation

To assess how well the mapping techniques performed, validation was conducted using GPS points collected in the field. Both spectral and LiDAR workflows resulted in maps representing the landscape categorized into a binary permafrost/no permafrost delineation that were easily validated using prime multiplication. The LiDAR workflow was validated using the 333 GPS points collected in the field (Figure 5). Validation of the spectral methods was conducted using the 67 GPS points collected in the field that occurred within the spectral extent (Figure 5), as well as the permafrost map created from the LiDAR workflow. Any change from 2007 to 2009 was considered minimal at this mapping resolution (1m), and the LiDAR provided a more extensive validation dataset for measuring the success of the spectral techniques compared to the relatively sparse GPS points. Since the LiDAR extent did not completely overlay the AOI, only the top half of the AOI could be validated using the LiDAR.

Validation was performed using prime number multiplication. This entailed classifying the truth values as 1 and 3, and the mapped values as 5 and 7. When multiplied together, the combination of primes resulted in unique values for each combination. This was used to assess whether the given value was correctly mapped as either permafrost or not permafrost, or incorrectly mapped as an error of omission or an error of commission (Table 2). Error of omission occurred when permafrost was present in actuality, but the mapping effort fails to map that area as permafrost, and *vice versa* for error of commission. The percent error was also calculated for each workflow as a metric of how well the model performed in mapping permafrost specifically (Equation 2). This calculation highlighted the error in mapping the permafrost explicitly, not just the error in mapping the landscape as a whole.

Table 2. Example of logic used for validation, where prime multiplication results in unique values for every outcome.

Hypothetical Outcome	Truth → Mapped	Truth	Mapped	Output
Absent	No Permafrost → No Permafrost	1	7	7
Present	Permafrost → Permafrost	3	5	15
Omission	Permafrost →No Permafrost	3	7	21
Commission	No Permafrost → Permafrost	1	5	5

Equation 2. Equation for calculating percent error of permafrost mapped.

$$\%\text{Error}_{\text{Permafrost}} = \frac{|P_{mapped} - P_{expected}|}{P_{expected}} * 100$$

Where P_{mapped} = the amount of permafrost mapped,
And $P_{expected}$ = the amount of permafrost expected to be mapped

Or in terms of the validation performed:

$$\%\text{Error}_{\text{Permafrost}} = \frac{|(Present + Commission) - (Present + Omission)|}{(Present + Omission)} * 100$$

By using the LiDAR output map as validation for the spectral mapping, residual error from the LiDAR analysis propagated through to the spectral analysis. To account for this, the probability that the spectral mapping technique was correct given that the spectral and the LiDAR agreed was calculated (Equation 3). This error propagation could only be calculated using the validation points that were coincident between the LiDAR validation and the spectral validation sets (n=56), which limited its power. Note that this was not an adjustment to the validation values found by validating with the LiDAR output map, but stood alone as an estimate

of the probability that the spectral mapping effort was correct given the LiDAR mapping effort's validation.

Equation 3. Probability calculation that the spectral mapping methods were correct in the context of error introduced from the LIDAR mapping method when validating the spectral workflows with the output of the LiDAR Workflow.

$$P(Spectral_{correct}) = P(Agrees_{LiDAR}|LiDAR_{correct})xP(LiDAR_{correct}) + P(Disagrees_{LiDAR}|LiDAR_{incorrect})xP(LiDAR_{incorrect})$$

2.6 Comparison Over Time

To assess changes in permafrost distribution and the reproducibility of the mapping workflows across time and spectral sensors, the automated spectral mapping workflows were applied to the remaining four sets of imagery (1988, 2004, 2013, and 2014) (Table 1). The fraction of the landscape mapped as permafrost and the percent error of observed permafrost were then compared among years to determine the viability of measuring rates of thermokarst and landscape change with these methods.

3. RESULTS

The following provides a brief summary of transect profiles taken in the field, results of mapping techniques from both LiDAR and spectral data, and a comparison of how well the spectral methods perform on imagery from different years. The fieldwork summary focuses on the transects probed, and the thaw depths collected. The mapping results focus on the percent accuracy of mapping the landscape (i.e. how well the model performed in mapping the landscape), especially in context of the percent error of mapping permafrost (i.e. how well the model performed in mapping permafrost explicitly). This distinction is noteworthy, and should be considered carefully. Finally, the comparison of the spectral methods through time highlights the reproducibility of the mapping efforts.

3.1 Transect Profiles

Of the nine transects sampled in the field, seven lay within the LiDAR swath, and six within the spectral mapping AOI. A total of 493 thaw depths were measured over 677 m of transect running across the permafrost plateau margins. There were eleven distinct ecotypes encountered in the field, but were consolidated for analysis to eight ecotypes to ensure sample sizes larger than ten probes. The ecotypes analyzed include: Lowland Moist Graminoid Shrub Meadow (LMGSM), Lowland Wet Graminoid Shrub Meadow (LWGSM), Lowland Wet Sedge Meadow[3] (LWSM), Lowland Wet Sedge-Shrub Meadow (LWSSM), Riverine Moist Graminoid Shrub Meadow (RMGSM), Thermokarst Pits[4] (TP), Water (W), and Wrack Lines (WL) from previous storm surges. Permafrost was encountered in 68.9% of the sample sites, which can be broken down by ecotype (Table 3). When thaw depth was analyzed by ecotype, permafrost was rarely encountered in the RMGSM (n=23), LWSSM (n=60), and LWGSM (n=35) ecotypes; and no permafrost was encountered at all in the Water class (n=7) (Table 3and Figure 11). An ANOVA revealed that there were significant differences between mean thaw depths in the various ecotypes ($\alpha = 0.5$; df = 6, 333; F = 33.36; p = <0.0001). The subsequent pairwise DTK

3. This group also included the Coastal Brackish Moist Graminoid-Willow Meadow and the Coastal Wet Graminoid Meadow ecotypes.
4. This group also included Thermokarst Moats.

test found that the LWSM was statistically different from the LWGSM, the RMGSM, and the TP at a 95% confidence level.

Field probing did not overlap completely with the LiDAR swath, but where probing did overlap, the mean elevation was 2.43 m above msl. These elevations were also analyzed by ecotype (Table 4 and Figure 12). The ANOVA conducted on elevation above msl also found significant differences between ecotypes ($\alpha = 0.5$; df = 7, 424; F = 23.99; p = <0.0001). The subsequent DTK test found the LMGSM statistically different from every ecotype except the TP and the WL; the RMGSM statistically different from the TP, the LWSSM, and the LWGSM; and the TP statistically different from the LWSM, the RMGSM, and the LWGSM.

Table 3. Percent permafrost encountered during probing by ecotype.

Ecotype	**Percent Permafrost**
W (n=7)	0.0%
LWGSM (n=35)	5.7%
LWSSM (n=60)	10.0%
RMGSM (n=23)	21.7%
LWSM (n=40)	40.0%
TP (n=21)	85.7%
LMGSM (n=292)	94.9%
WL (n=15)	100.0%

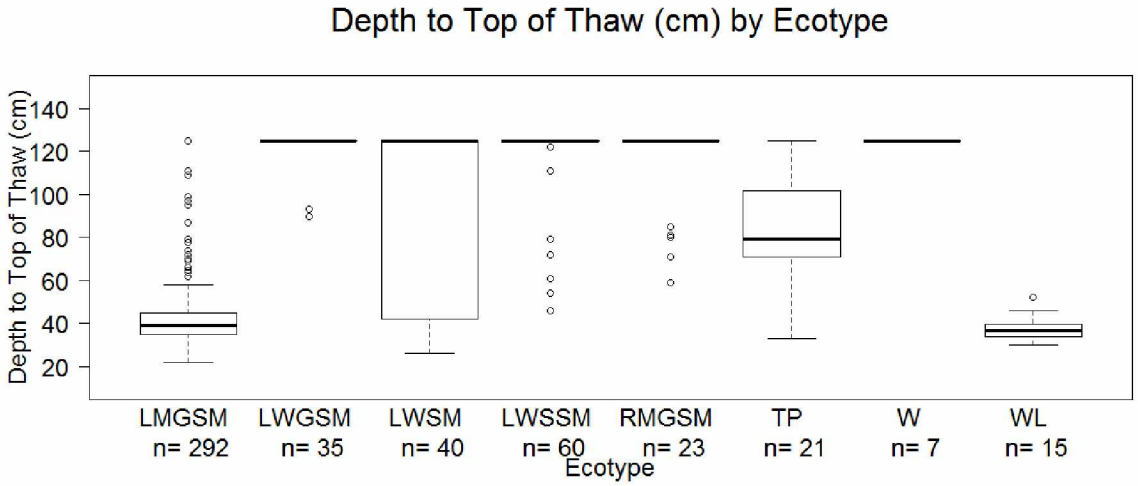

Figure 11. Thaw Depth (m) by ecotype. Bold horizontal lines show the median thaw depth for each transect, the boxes show the Inter-Quartile Range (IQR)of the thaw data, and the whiskers show 1.5 * IQR ± 1st and 3rd quartiles, respectively. Circles above the whiskers show outliers in the transect as defined by the statistical programming language R (R Development Core Team 2016). Note that the maximum thaw depth was the length of the thaw probe (1.25 m), and indicates lack of permafrost in the majority of cases.

Table 4. Mean elevation (m above msl) by each ecotype probed during fieldwork.

Ecotype	**Mean Elevation (m above msl)**
RMGSM (n=23)	2.06
LWGSM (n=35)	2.21
LWSM (n=34)	2.21
W (n=6)	2.22
LWSSM (n=54)	2.27
WL (n=7)	2.34
TP (n=21)	2.52
LMGSM (n=252)	2.56

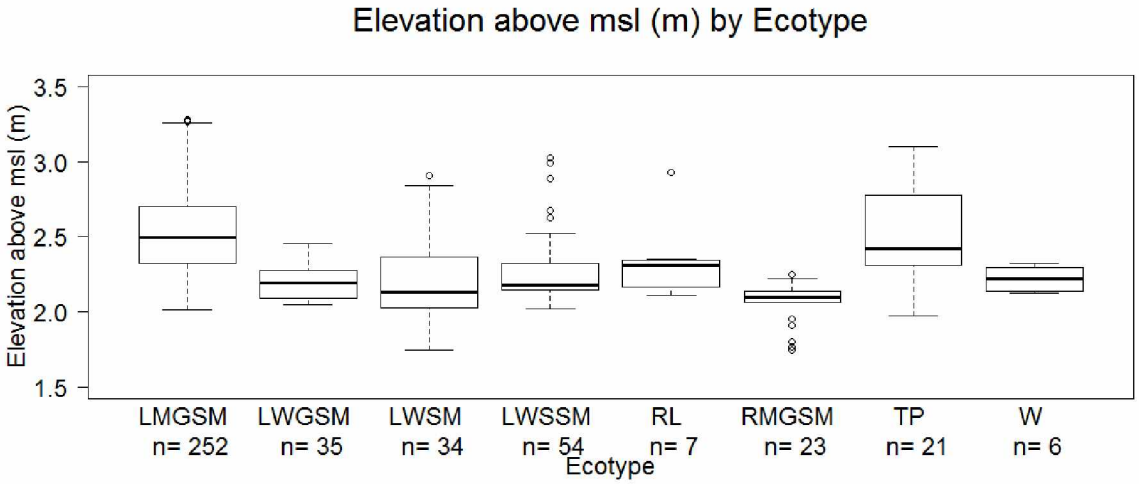

Figure 12. Elevation (m above msl) of probing sites along field transects by ecotype. Bold horizontal lines show the median thaw depth for each transect, the boxes show the IQR of the thaw data, and the whiskers show 1.5 * IQR ± 1st and 3rd quartiles, respectively. Circles above and below the whiskers show outliers in the transect as defined by R.

Table 5. Descriptive statistics for thaw depths (m) by ecotype.

Ecotype	Mean (m)	Standard Deviation (m)	Median (m)	Maximum (m)	Minimum (m)
WL (n=15)	0.39	0.07	0.37	0.52	0.30
LWSM (n=40)	0.40	0.10	0.38	0.63	0.26
LMGSM (n=292)	0.42	0.12	0.38	1.11	0.22
TP (n=21)	0.75	0.26	0.78	1.11	0.33
RMGSM (n=23)	0.75	0.10	0.80	0.85	0.59
LWSSM (n=60)	0.78	0.29	0.72	1.22	0.46
LWGSM (n=35)	0.92	0.02	0.92	0.93	0.90

Table 6 Descriptive statistics for elevation (m above msl) by ecotype..

Ecotype	Mean (m above msl)	Standard Deviation (m above msl)	Median (m above msl)	Maximum (m above msl)	Minimum (m above msl)
RMGSM (n=23)	2.06	0.14	2.10	2.25	1.75
LWGSM (n=35)	2.21	0.12	2.19	2.46	2.05
LWSM (n=34)	2.21	0.26	2.13	2.91	1.74
W (n=6)	2.22	0.09	2.22	2.32	2.12
LWSSM (n=54)	2.27	0.22	2.18	3.03	2.02
WL (n=7)	2.34	0.28	2.31	2.93	2.11
TP (n=21)	2.52	0.34	2.42	3.10	1.97
LMGSM (n=252)	2.56	0.30	2.50	3.28	2.01

Permafrost thickness measurements (top of frost – bottom of frost) were collected for 19 of the sample points (3.9%), which all occurred at the transition from permafrost plateau to coastal meadow where the frost was thin enough to break through manually. The average thickness of frost at these points was 26.1 cm (standard deviation 15.7 cm), with a maximum thickness of 62.0 cm and a minimum thickness of 3.0 cm.

Further probing found that permafrost was still present under most shallow ponds and thermokarst pits on the plateaus (85.7% permafrost occurrence) despite the presence of *Ranuculus pallasii*, *Hippuris tetraphylla*, and other indicators of advanced stages of thermokarst. Along the margins of the plateaus, it was found that areas with driftwood and rack line cover were generally underlain with permafrost, as well. A talik (area of perennially thawed ground within the permafrost) was also found at one location along Transect 5 under dense driftwood deposits. At this sampling site, 8.0 cm of seasonal frost was found at a depth of 52.0 cm, with the top of the actual permafrost at a depth of 86.0 cm. Another discovery of note was the presence of a small ice wedge in the southern portion of the LiDAR swath within the AOI (Figure 13).

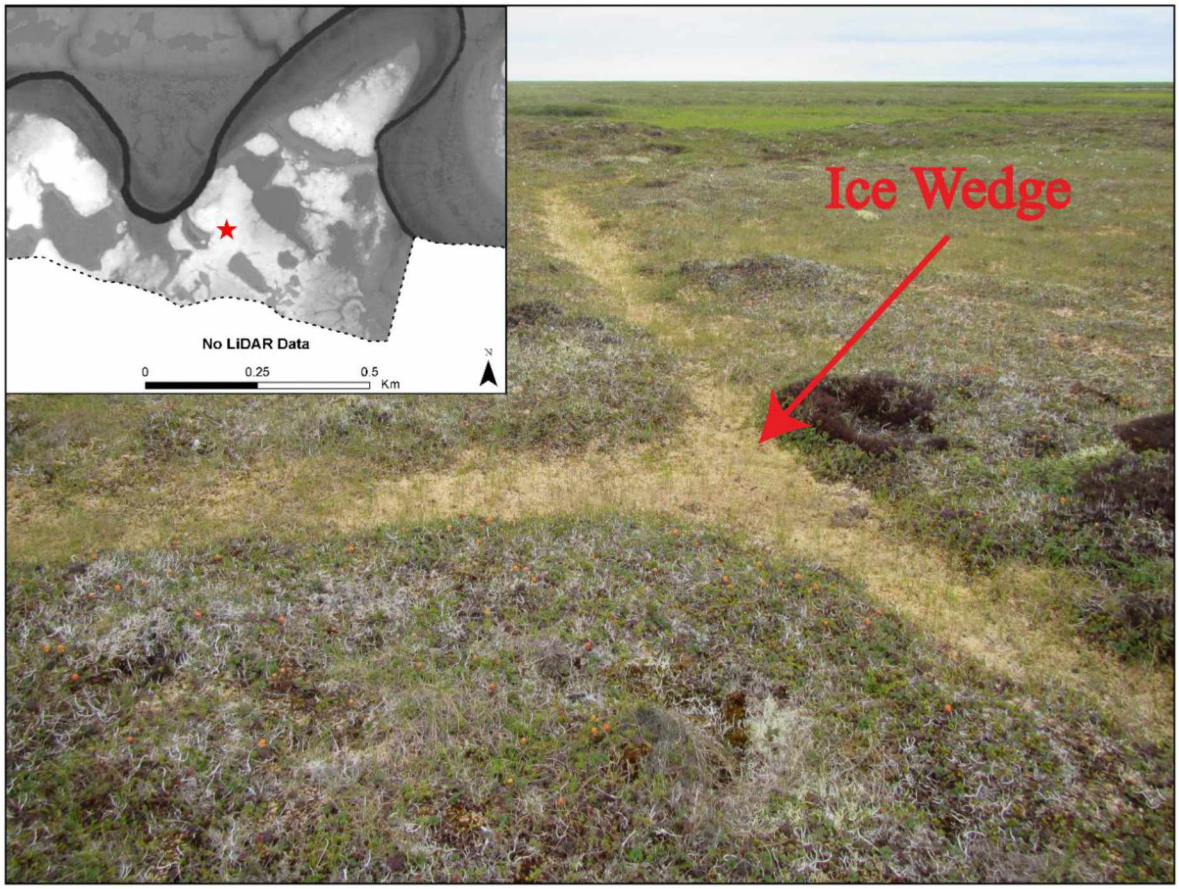

Figure 13. Ice wedge found near the southern boundary of the LiDAR swath within the spectral mapping AOI.

In all, 29 distinct transitions from permafrost to coastal meadow were observed along the transects, and 27 within the LiDAR swath. The average elevation of these boundaries extracted from the LiDAR DEM was 2.3 m above msl, with a standard deviation of 0.2 m. Minimum and maximum boundary elevations were 2.0 m above msl and 2.8 m above msl, respectively.

3.2 LiDAR Mapping

The proposed LiDAR mapping method that used 2.5 m above msl (mean + 1 standard deviation) as a threshold produced a map resulting in accurate representation of the permafrost on the delta (Figure 14). Validation from the 333 GPS points within the LiDAR swath showed 94.9% accuracy in mapping the landscape (Table 7). Error of omission for the model was 4.2%, and the error of commission only 0.9%.

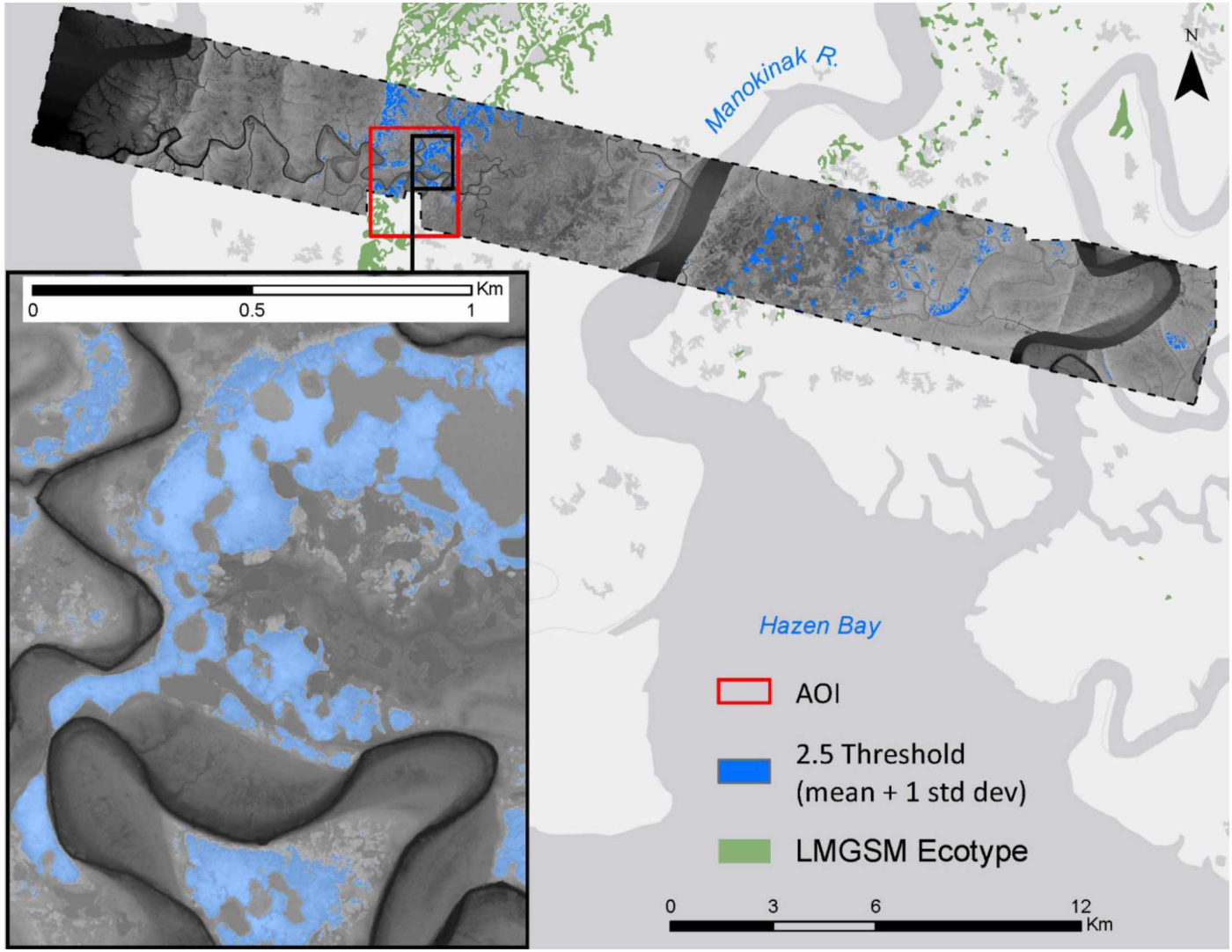

Figure 14. Result of LiDAR mapping with 2.5 m above msl (mean + 1 standard deviation) threshold. The LMGSM is shown in the background as green, and the 2009 LiDAR extent is shown with a dashed line. The inset enlarges a portion of the spectral mapping AOI to show the result in greater detail

Table 7. LiDAR model accuracy based upon 333 GPS points taken in the field for both the 2.3 m above msl (mean) and 2.5 m above msl (mean + 1 standard deviation) thresholds. The total model accuracy and error is shown in bold.

	2.5 Threshold (Mean + 1 std dev)	**2.3 Threshold (Mean)**
Total Accuracy	**94.9%**	**94.6%**
Absent	77.8%	75.7%
Present	17.1%	18.9%
Total Error	**5.1%**	**5.4%**
Omission	4.2%	2.4%
Commission	0.9%	3.0%

The permafrost map derived from the 2.3 m above msl (mean) threshold performed roughly the same (94.6% accuracy) as the permafrost map derived from the 2.5 m above msl (mean + 1 standard deviation) threshold (94.9% accuracy). However, visual comparison of the two methods indicates the 2.5 m above msl threshold was a more realistic representation of permafrost in the AOI, when areas beyond the validation points were considered (Figure 15). The percent error calculated for mapping permafrost also elucidates the difference between these models: the 2.5 m above msl threshold omits 19.7% of the permafrost (and commits 4.2%), and the 2.30 m above msl threshold only omits 11.3% of the permafrost (but commits 14.1%) (Table 8).

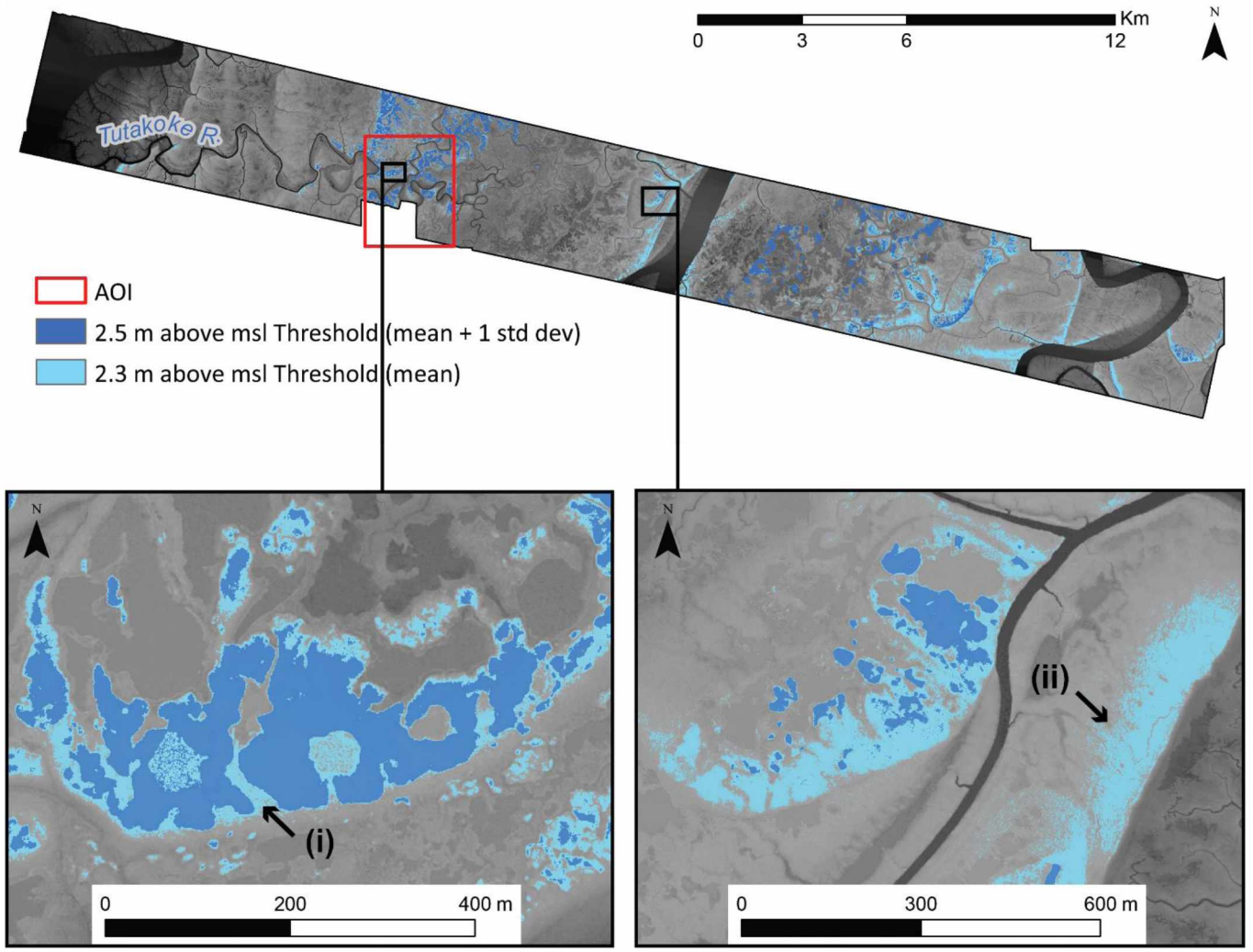

Figure 15. Comparison of LiDAR thresholds for mapping permafrost. The 2.5 m above msl (mean + 1 standard deviation) threshold is shown in dark blue, and the 2.3 m above msl (mean) threshold is shown in light blue. Insets enlarge results to see errors of commission highlighted with (i) and (ii) at different points along the LiDAR swath.

Table 8. Percent error of mapping permafrost in the LiDAR mapping workflow. Errors of omission and commission explain how much of the permafrost on the landscape was missed or added, respectively, in relation to how much permafrost is actually on the landscape. The total percent error is the difference between the percent error of omission and commission.

Error Type	2.5 Threshold (Mean + 1 std dev)	2.3 Threshold (Mean)
Total	**15.5%**	**2.8%**
Omission	19.7%	11.3%
Commission	4.2%	14.1%

The logistic regression found that elevation was a highly significant indicator of near-surface permafrost in the region ($z = 9.056$, $p = <0.0001$). This shows that there is higher likelihood of encountering near-surface permafrost at higher elevations, and lower likelihood of encountering near-surface permafrost at lower elevations (Table 9). Both these instances had low uncertainties in the probability calculation (values << or >> 50%), whereas the mid-elevations showed the highest uncertainties (values ~50%) in the probability calculation. These uncertainties and probabilities are clearly seen graphically when the logistic regression is plotted (Figure 16), as well as spatially when the probabilities are mapped from the 2009 LiDAR swath (Figure 17). When a threshold of 0.90 probability was selected as a threshold for mapping, the binary map (permafrost/no permafrost) produced showed accuracies slightly lower, but still comparable to the 2.3 m above msl (mean) threshold (Table 10). However, distinction between the two methods can be seen in the types of errors committed in mapping. Whereas the 2.3 m above msl (mean) threshold had mixed errors (omission: 2.4%, commission: 3.0%), with slightly more error of commission; the 0.9 probability threshold committed more errors of omission (5.4%) and hardly any errors of commission (0.3%).

Table 9. Predicted probability of near-surface permafrost calculated for every 0.1 m elevation bin. The table displays the total number of observations that were and were not permafrost in each elevation bin, the total number of observations in each elevation bin (n), and the predicted probability of near surface permafrost calculated from the logistic regression.

Elevation	No Permafrost	Permafrost	n	Predicted Probability of Near Surface Permafrost
1.7 - 1.8	4	0	4	**0.04**
1.8 - 1.9	1	0	1	**0.07**
1.9 - 2.0	6	0	6	**0.13**
2.0 - 2.1	34	8	42	**0.22**
2.1 - 2.2	43	17	60	**0.36**
2.2 - 2.3	23	38	61	**0.53**
2.3 - 2.4	18	46	64	**0.69**
2.4 - 2.5	10	31	41	**0.81**
2.5 - 2.6	3	38	41	**0.89**
2.6 - 2.7	1	33	34	**0.94**
2.7 - 2.8	0	11	11	**0.97**
2.8 - 2.9	1	16	17	**0.98**
2.9 - 3.0	1	14	15	**0.99**
3.0 - 3.1	1	16	17	**1.00**
3.1 - 3.2	0	7	7	**1.00**
3.2 - 3.3	0	11	11	**1.00**

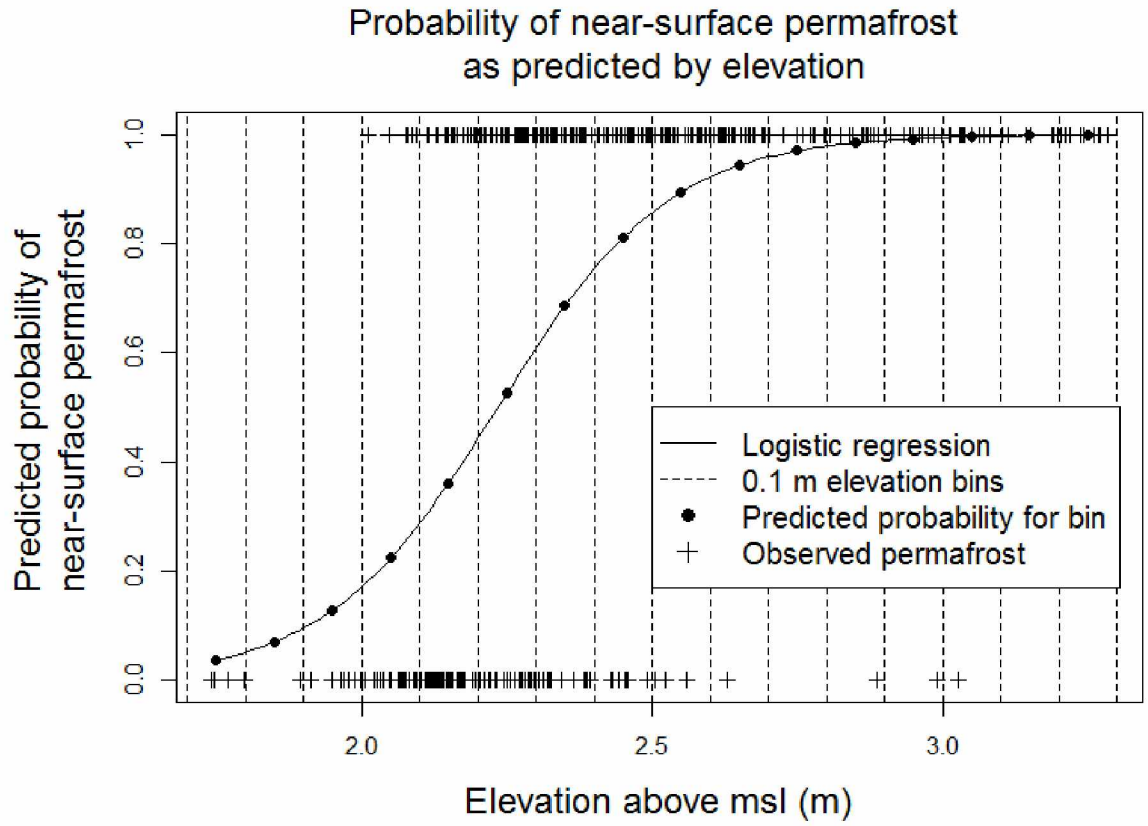

Figure 16. Probability of near-surface permafrost as predicted by elevation. The logistic regression is shown as a solid black line. The elevation bins are shown with dashed black lines, and the values predicted for each bin from the logistic regression are shown with black circles. The plus signs show permafrost observations (1 = permafrost, 0 = no permafrost) plotted by their elevation. Presence of permafrost only occurs at the top of the plot (probability = 1), and absence of permafrost only occurs at the bottom of the plot (probability = 0), because of the binomial nature of sampling (i.e. no sites were considered "half permafrost"). The density of permafrost encounters is skewed towards higher elevations, with few observations below 2.1 m above msl, and no observations below 2.0 m above msl. Conversely, the density of samples that did not encounter permafrost were generally found at lower elevations above msl, with few observations above 2.5 m above msl, and no observations above 3.1 m above msl.

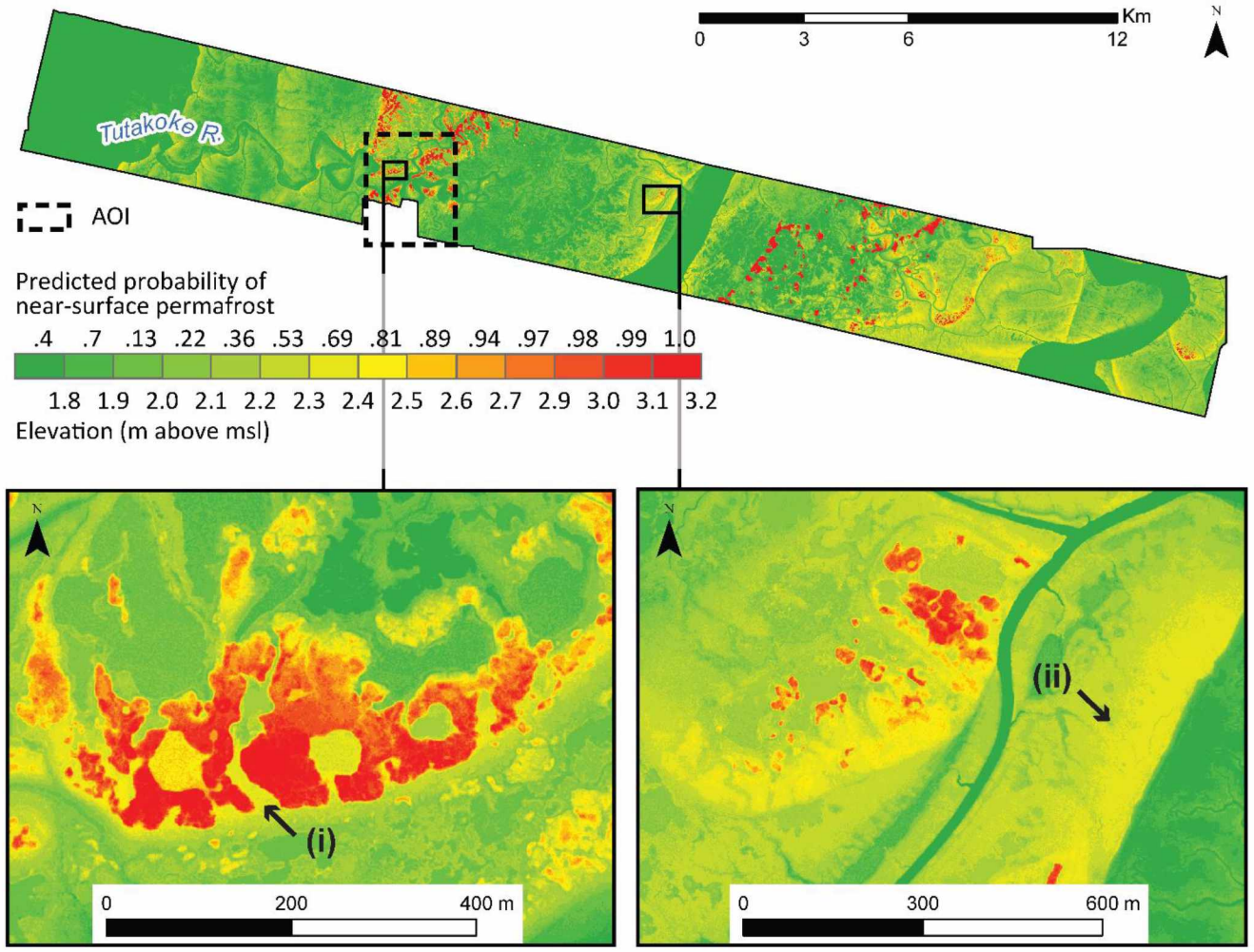

Figure 17. Map of the predicted near-surface permafrost probability calculated by 0.1 m elevation bins. High likelihood of near-surface permafrost areas (red) are clearly distinct from low likelihood of near-surface permafrost areas (green), with the areas of uncertainty (yellow) mostly along the margins of the permafrost plateaus. Insets enlarge results to show where previous errors of commission (Figure 15 (i) and (ii)) become distinct by incorporating the logistic regression.

Table 10. LiDAR model accuracy based upon 333 GPS points taken in the field for a 0.9 probability threshold. The total model accuracy and error are shown in bold.

	0.9 Probability Threshold
Total Accuracy	**94.3%**
Absent	78.4%
Present	15.9%
Total Error	**5.7%**
Omission	5.4%
Commission	0.3%

3.3 Spectral Mapping

Though not as accurate as the LiDAR mapping workflow, both spectral workflows resulted in fairly accurate representations of permafrost extent using the 2007 IKONOS scene. Validation performed with the field GPS points resulted in lower mapping accuracies overall than validation performed with the result of the LiDAR mapping. The 62 GPS points within the spectral mapping AOI used for validation resulted in total model accuracies between 61.3% and 79.0% depending on the workflow and threshold selected (Table 11). However, when validating with the permafrost map derived from the LiDAR workflow, model accuracies ranged from 78.1% to 89.4% (Table 12). Error in both validation methods mostly came from errors of omission, with the exception of the automated Workflow 1 having a higher error of commission when validating with the LiDAR output map.

Table 11. Results of spectral mapping validation using GPS points collected in the field.

	Workflow 1		Workflow 2	
	Threshold: 5.3	Threshold: mean	Threshold: 5.3	Threshold: mean
Total Accuracy	**62.9%**	**61.3%**	**79.0%**	**67.7%**
Absent	25.8%	9.7%	27.4%	27.4%
Present	37.1%	51.6%	51.6%	40.3%
Total Error	**37.1%**	**38.7%**	**21.0%**	**32.4%**
Omission	35.5%	21.0%	21.0%	32.3%
Commission	1.6%	17.7%	0.0%	0.0%

Table 12. Results of spectral mapping validation using LiDAR output map.

	Workflow 1		Workflow 2	
	Threshold: 5.3	Threshold: mean	Threshold: 5.3	Threshold: mean
Total Accuracy	**89.4%**	**78.1%**	**88.1%**	**87.2%**
Absent	78.6%	60.9%	77.3%	79.7%
Present	10.8%	17.2%	10.8%	7.5%
Total Error	**10.6%**	**21.9%**	**12.0%**	**12.8%**
Omission	7.7%	1.3%	7.7%	11.1%
Commission	2.9%	20.6%	4.2%	1.8%

In terms of percent error, Workflow 1 consistently had the highest error of commission (Table 13). Conversely, Workflow 2 reduced errors of commission well, but had the highest errors of omission (Table 13). It is noteworthy that Workflow 2 had an omission error of 0.00% when validated with the GPS points, and the automated Workflow 1 had a commission error of 110.94% when validated using the LiDAR output.

Table 13. Percent error of mapping permafrost in the spectral mapping workflows, as validated by GPS and LiDAR output map.

		Workflow 1		Workflow 2	
		Threshold: 5.3	Threshold: mean	Threshold: 5.3	Threshold: mean
GPS Validation	**Total % Error**	**51.1%**	**4.5%**	**28.9%**	**44.4%**
	Omission	48.9%	28.9%	28.9%	44.4%
	Commission	2.2%	24.4%	0.00%	0.00%
LiDAR Validation	**Total % Error**	**26.0%**	**-103.9%**	**19.1%**	**50.3%**
	Omission	41.6%	7.0%	41.8%	59.7%
	Commission	15.6%	110.9%	22.7%	9.4%

For threshold selection, manual selection produced better results than automating selection using the mean. Coincidentally, a cutoff of 5.3 for both workflows produced the best accuracy in mapping the overall landscape. As a note on units, the histogram of Workflow 2 did not have units because PCAs are unitless; and the histogram for Workflow 1 had units of radiance^3 ($[W/(m^2*sr)]^3$), although it provides little information in terms of physical characteristics of the surface. This manual delineation resulted in little difference from the mean in Workflow 2, but in Workflow 1 resulted in more than 11% increase in mapping accuracy (as validated using the LiDAR output).

To account for error propagated through the analysis from the LiDAR workflow, the probability that the spectral mapping was correct given whether the LiDAR was correct or incorrect (Equation 3) was calculated from the coincident validation points. This calculation resulted in probabilities (Table 14) that were similar in magnitude to the validation conducted with the field GPS validation points (Table 11).

Table 14. Probability calculated that the spectral mapping workflows are correct given the error in the LiDAR mapping workflow when validating the spectral workflows using the LiDAR output map.

	Workflow 1		**Workflow 2**	
	Threshold: 5.3	Threshold: mean	Threshold: 5.3	Threshold: mean
Probability $Spectral_{correct} \mid LiDAR_{correct}$	0.61	0.59	0.59	0.70

To visualize how each workflow and threshold performed in comparison to each other, the manual and automated products of both workflows were displayed (Figure 18). Similarly, visualizing the mapping products in context of the landscape using the LiDAR data helps to interpret the results (Figure 19).

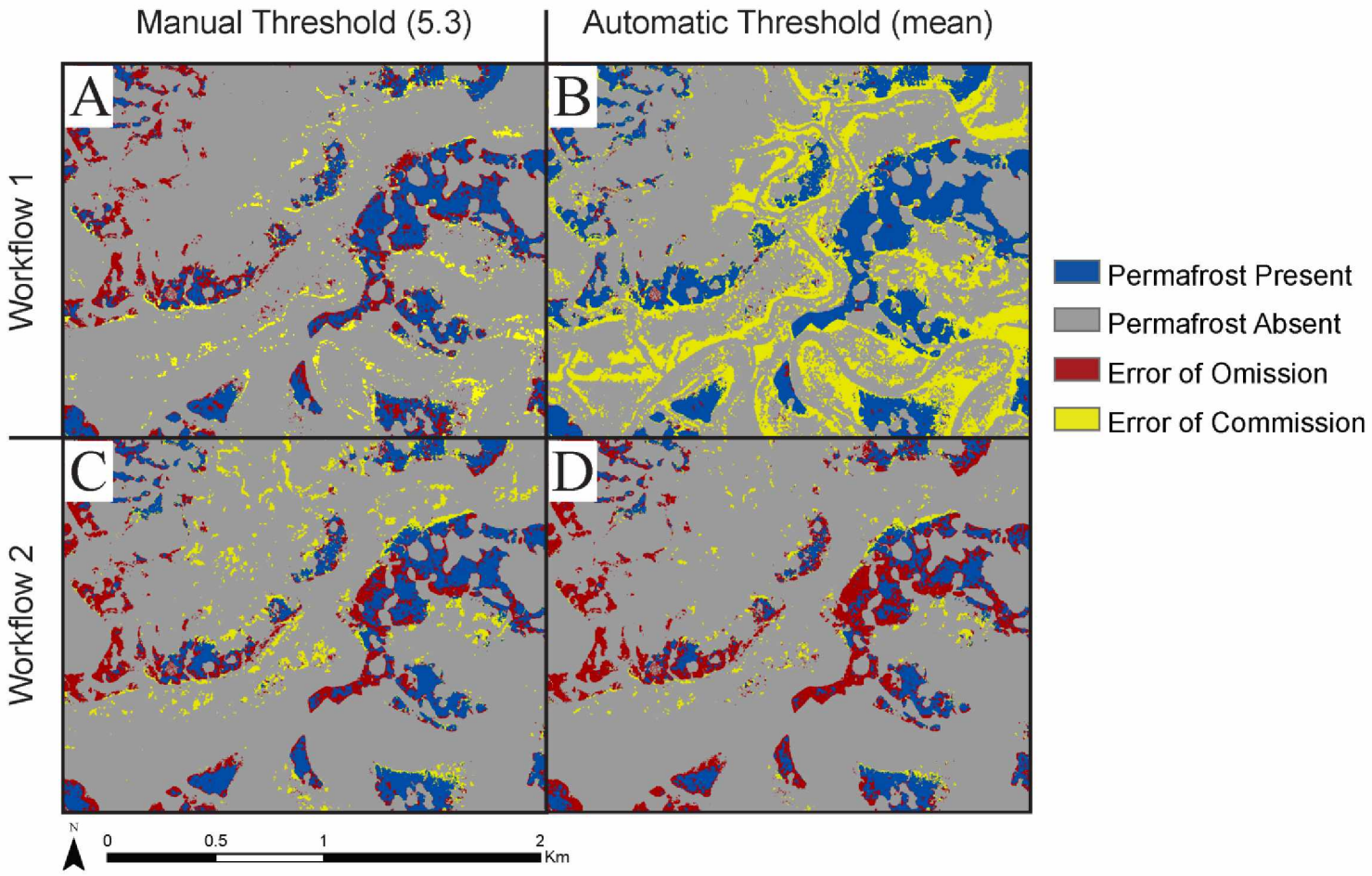

Figure 18. Comparative maps of validation based on LiDAR output map: correctly mapped permafrost (blue), correctly mapped non-permafrost (grey), error of omission (red), and error of commission (yellow) is shown for A) Workflow 1, manual threshold selection, B) Workflow 1, automated threshold selection, C) Workflow 2, manual threshold selection, and D) Workflow 2, automated threshold selection.

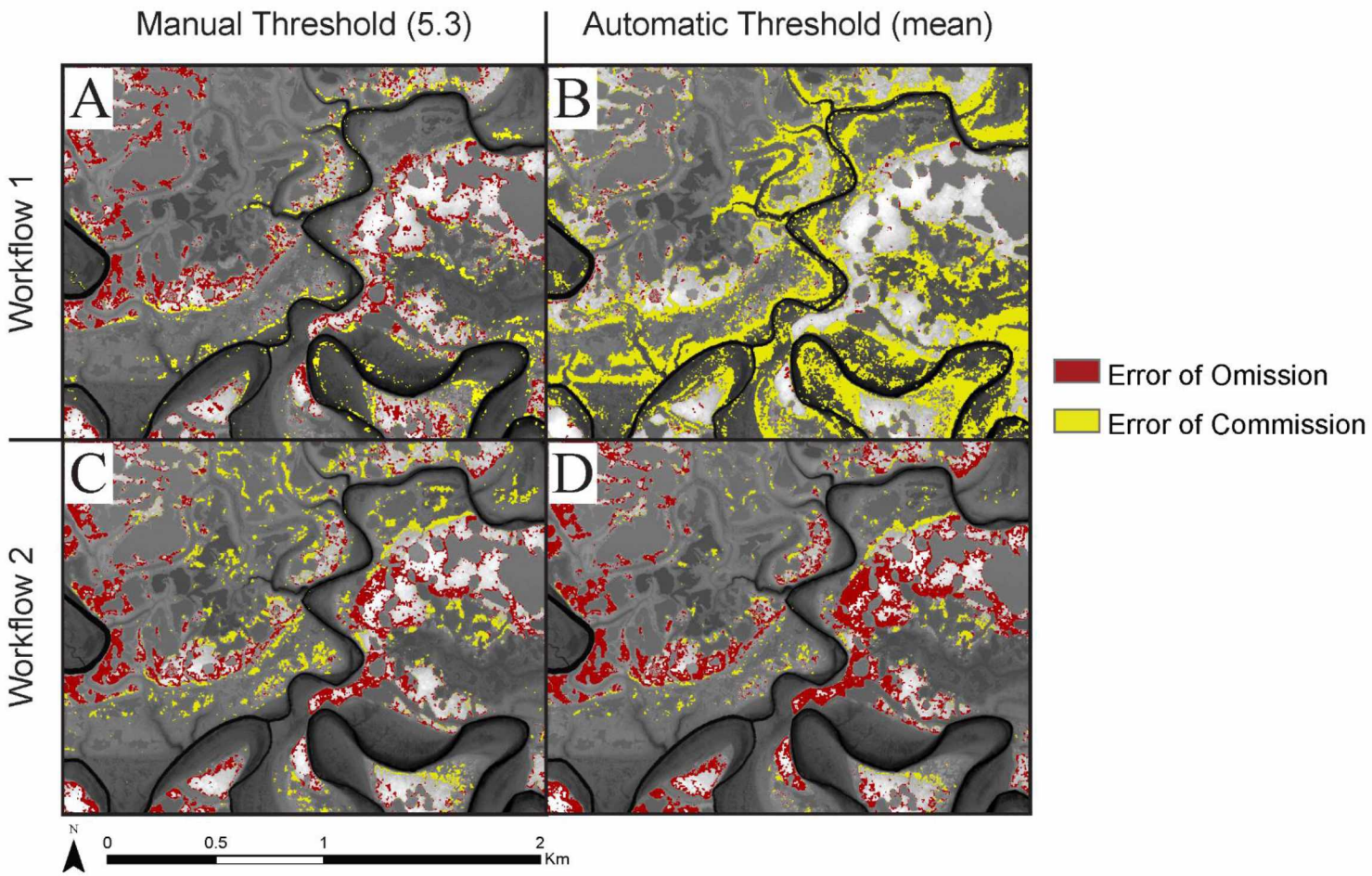

Figure 19. Spectral permafrost mapping error in context of the landscape for A) Workflow 1, manual threshold selection, B) Workflow 1, automated threshold selection, C) Workflow 2, manual threshold selection, and D) Workflow 2, automated threshold selection. Error of omission is shown in red, and error of commission is shown in yellow over the LiDAR data.

3.4 Comparison Over Time

When the automated spectral mapping workflows were applied to images from other dates (1988, 2004, 2013, and 2014), there was substantial variability in permafrost extent among years. The percent of the landscape mapped as permafrost and the percent error in mapping permafrost were used as indicators of how consistently the mapping algorithms performed over time. The automated Workflow 1 drastically overestimated permafrost cover, with 40-60% of the landscape mapped as permafrost, and percent errors over 200% for some years (Figure 20). The automated Workflow 2 resulted in similar variability, but lower percentages. Landscape percentages calculated were within a more realistic range of 12-24%, and percent errors were only as high as ~30% (Figure 21). In both cases, the large variance in percentages made comparing maps across time difficult, so no further temporal analysis of trends was conducted.

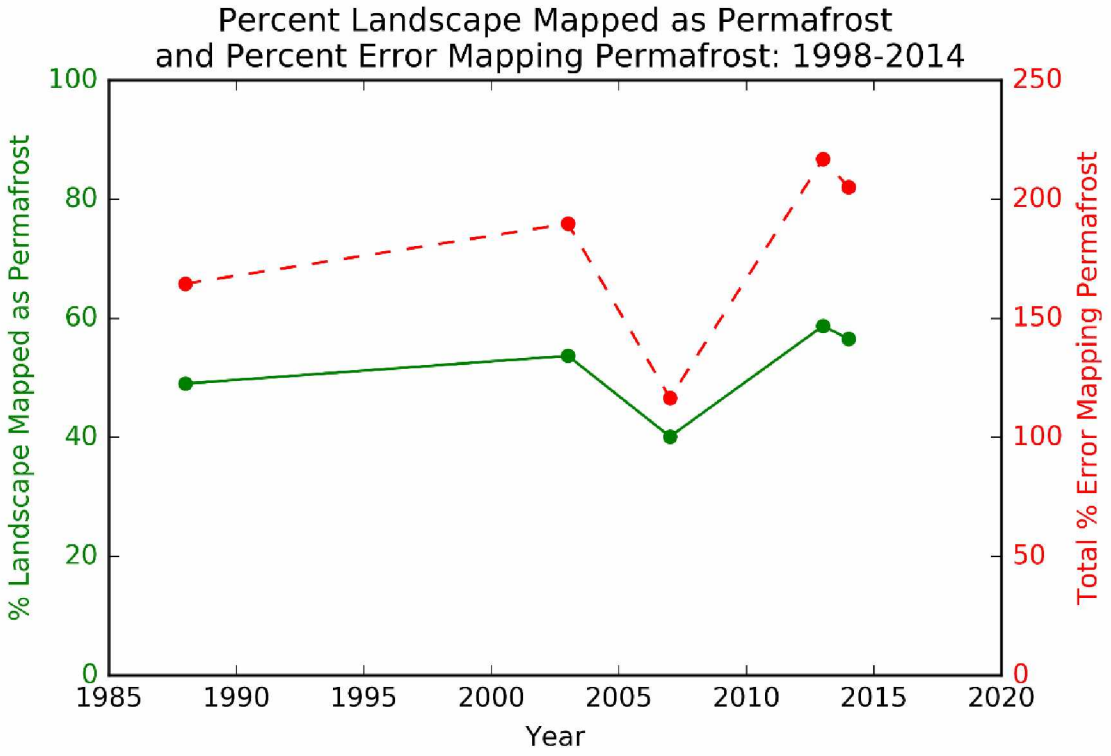

Figure 20. Percent of landscape mapped as permafrost (green) and percent error in mapping permafrost (red) for Workflow 1 from 1988-2014. The large variability in the data show the inconsistency of the mapping algorithm across time and sensors. The percent of the landscape mapped as permafrost (y-axis) is close to double true permafrost cover, giving context to the extremely high percent error in mapping permafrost (second y-axis).

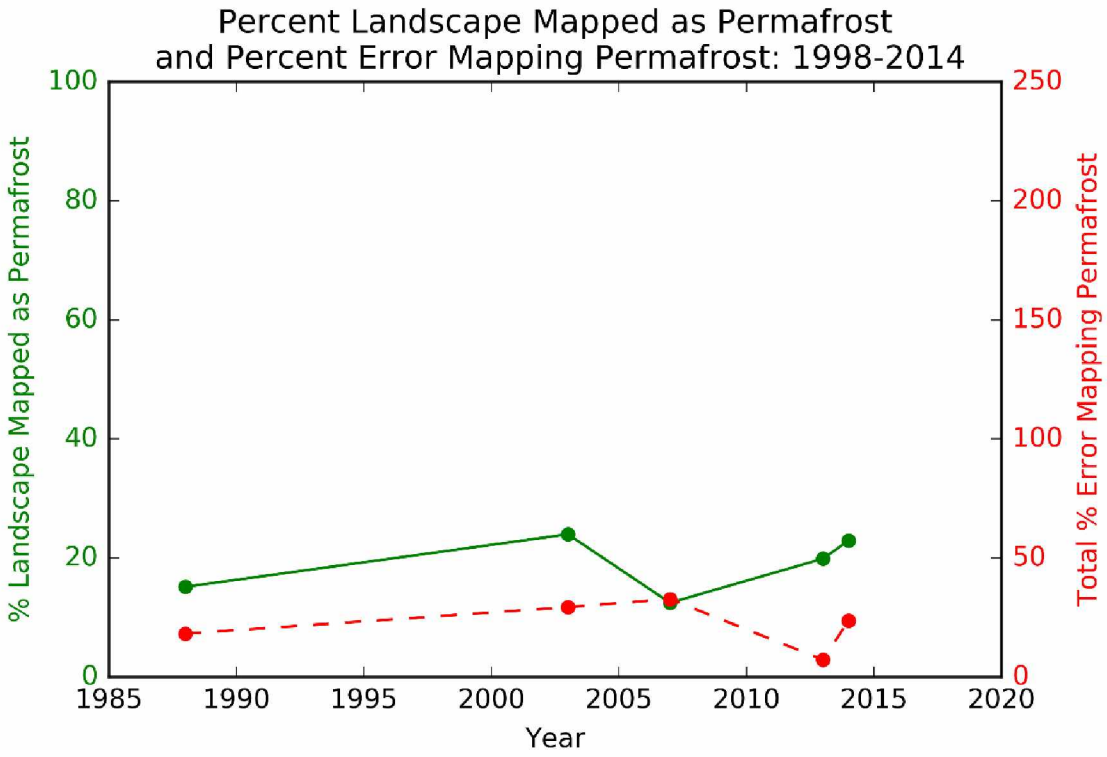

Figure 21. Percent of landscape mapped as permafrost (green) and percent error in mapping permafrost (red) for Workflow 2 from 1988-2014. The large variability in the data show the inconsistency of the mapping algorithm across time and sensors. The percent of the landscape mapped as permafrost (y-axis) is more realistic than the results of Workflow 1, which is reflected in the percent error in mapping permafrost (second y-axis). Note axis ranges are the same as Figure 20.

4. DISCUSSION

Overall, mapping the permafrost on the YKD was not an easy task. The LiDAR mapping workflow clearly performed better than the spectral workflows, but problems with both mapping algorithms remain. Regional implementation of the LiDAR mapping workflow would be monetarily and computationally costly. While the spectral workflows present a much cheaper alternative, variable results raise questions about the overall replicability in mapping permafrost spectrally. Therefore, LiDAR is likely the best method for monitoring permafrost on the YKD, given its higher accuracy, and its expanding role in the flat region.

4.1 Landscape Characteristics

It is highly unlikely that permafrost is present in the areas that were probed but found no frozen ground within the top 1.25 m. Previous studies (Jorgenson 2000, Jorgenson and Ely 2001, Jorgenson and Roth 2010) have probed down to 2.5 m in similar areas, and have consistently found no permafrost. This condition, coupled with the close correlation between permafrost areas and elevation, makes the YKD a unique region in which to study permafrost. Because there is a high certainty that there is no permafrost where there are no plateaus, this study site is uniquely suited to mapping permafrost based solely on high resolution elevation datasets. Thus, LiDAR is a powerful mapping resource that this analysis has shown performs extremely well.

The YKD is likely unique in this aspect, due to the combination of climate, latitude, physiography, and vegetation cover. Similar arctic deltas, such as the Lena Delta or the Mackenzie Delta, lie further north, where colder climates result in widespread climate-driven permafrost distribution, even along the coast (Shur and Jorgenson 2007). Other areas of sporadic to isolated permafrost found in Interior Alaska and across the Arctic have similar climates, but landscapes are not as flat, and don't have interaction from coastal processes. The positive feedback loop that the slight elevation difference and the vegetation cover provide is not a unique phenomenon, but in context of the flat delta, makes it possible to identify permafrost with accuracy. Despite these limitations, exploring mapping techniques is justified by the overall size and importance of the YKD. This technique may prove to be useful in other landscapes when mapping at a large spatial scale. For example, collapse-scar bogs and other flat areas in Interior

Alaska such as the Tanana Flats are potentially flat enough that accretion of ground ice would create an identifiable topographic feature in the area.

The average elevation of the plateaus reported by Jorgenson and Ely (2001), 2.84 m above msl, agree in context with the elevations found for transitions in this study (2.5 m above sea level). Theoretically, the average elevation of permafrost boundaries should be slightly lower than the average elevation of the plateaus. In this case, the maximum boundary elevation calculated (2.82 m above msl) corresponds well with the mean elevation cited by Jorgenson and Ely (2001).

Identifying permafrost on the YKD seems easy because of the unique topographical and vegetative characteristics of the plateaus. However, the relative abundance of permafrost on the delta (~20% of the landscape) is also an important factor to consider when mapping. Panda et al. (2010) note that the success of mapping permafrost is generally "higher when a larger part of the study area is underlain by permafrost: regardless of the technique used, the accuracy drops as the extent of permafrost becomes limited". Since the YKD is mostly isolated to sporadic permafrost, precisely mapping permafrost extent is an inherently difficult task, but important given the vulnerability of the permafrost in the region to rising air temperatures and inland storm surges.

Where permafrost *is* present on the delta, it is found at relatively shallow depths. This is due to the insulative properties of vegetation and soils on the plateaus, and the subsequent organic layers found in the soil. The abundant mosses and lichens performing this service exemplify the theory of ecosystem-protected permafrost, introduced by Shur and Jorgenson (2007). Vegetation cover, such as the S*phagnum* peat and lichen present on the plateaus, absorbs moisture and provides an insulative layer that has low thermal conductivity in the summer, but subsequently freezes and has high thermal conductivity in the winter. This duality in thermal conductivity allows for heat exchange from the ground in the winter, but prevents penetration of heat from the atmosphere in the summer (Tyrtikov 1964). Soil moisture plays an important role in this process, as only moist soils will provide this insulation unlike the wetter soils found in the coastal meadows. Soils that are too wet result in higher heat transfer to the ground, resulting in unfavorable conditions for permafrost. On the flat delta, soil moisture is related to elevation, which can be seen in the mean elevation of each ecotype probed during fieldwork (Table 6). The analysis of frost depths by ecotype show that even subtle differences in soil moisture and vegetation type can lead to large differences in active layer thickness. For example, the

difference between the mean frost depth in the LMGSM (0.42 ± 0.12 m) and the LWGSM (0.92 ± 0.02 m) is 0.5 m.

Interactions from flooding contribute to thermo-erosional processes and can initiate thermokarst (Jorgenson and Ely 2001, Kokelj and Jorgenson 2013, Terenzi et al. 2014). Thus, the discovery that the WL group[5] had the shallowest average thaw depths came as a surprise, since wrack lines were originally assumed areas of permafrost degradation. Some of the thaw depths measured under the WL group were also likely seasonal frost (in particular the 0.3 m thaw depth observed), which helps to explain the shallow thaw depths. However, the majority of samples sites under the WL had hard, solid permafrost. The persistence of the permafrost may be due to negative feedback loops in the energy balance, where the higher albedo of the driftwood protects the permafrost by reflecting more of the sun's energy. However, the observed presence of a talik under the driftwood also indicates that thermokarst is occurring. This may indicate that despite its presence, permafrost under wrack lines is degrading from the initial disturbance of the storm that deposited the wrack. Alternatively, the presence of a talik underneath the wrack lines may come from lateral degradation of the permafrost, as the permafrost plateaus on the YKD generally degrade from the outside towards the center (e.g. thermokarst moats). Further monitoring of the permafrost under WL, in conjunction with the estimated age of the wrack deposit, is needed to fully understand the dynamics of the permafrost in these areas.

Not only is the permafrost shallow on the YKD, it is also likely thin. Areas of the YKD that currently have permafrost are relatively young compared to more stable permafrost on the North Slope, Interior Alaska, and other colder patches across the pan-Arctic. The dynamic processes of the Yukon and Kuskokwim rivers prevent stable permafrost formation on the landscape due to lateral movement of river channels and continuous deposition of sediment. The mouth of the Yukon River flowed south into the Gulf of Alaska during the late Pliocene, and swung northward to its current location from glacial damming during the Pleistocene (Duk-Rodkin et al. 2001). This movement, along with the movement in the Kuskokwim River's channel, demonstrates the mercurial nature of the YKD floodplain. Paleoecology records of past vegetation, as well as sea level reconstructions also constrain when permafrost would have

5. Do note that the WL group included wrack accumulations consisting of dead sedge and grass, not just large woody debris. This distinction may drive a binary distribution of thaw depths within this group.

developed on the coastal plain, since the region would have been too dynamic before ~6,000 years ago (Ager 1982, Fleming et al. 1998, Fleming 2000, Milne et al. 2005). Jorgenson and Ely (2001) suggest this permafrost is transient in nature, and that formation may have started as late as the Little Ice Age (250-700 years ago), based on the estimated permafrost thickness of 10 m.

Assuming that no seasonal frost was encountered during thaw probing, an idea of permafrost thickness can be gleaned from plotting the depth to the top of thaw, the depth to the bottom of thaw (where known), and the ground surface elevations in relation to sea level. Figure 22 annotates this plot with pictures of notable landscape characteristics that define the transition from LMGSM to the surrounding coastal meadows, as well as unique characteristics related to thaw depth and elevation. Permafrost thickness can be inferred from the height of the topographic break between the permafrost plateau and the surrounding coastal meadow, with the context of the ice types and relative abundance in the permafrost. Since there is only pore and segregated ice in the soil, the permafrost plateau thickness can be estimated to be ~10 m (Jorgenson 2000, Jorgenson and Ely 2001).

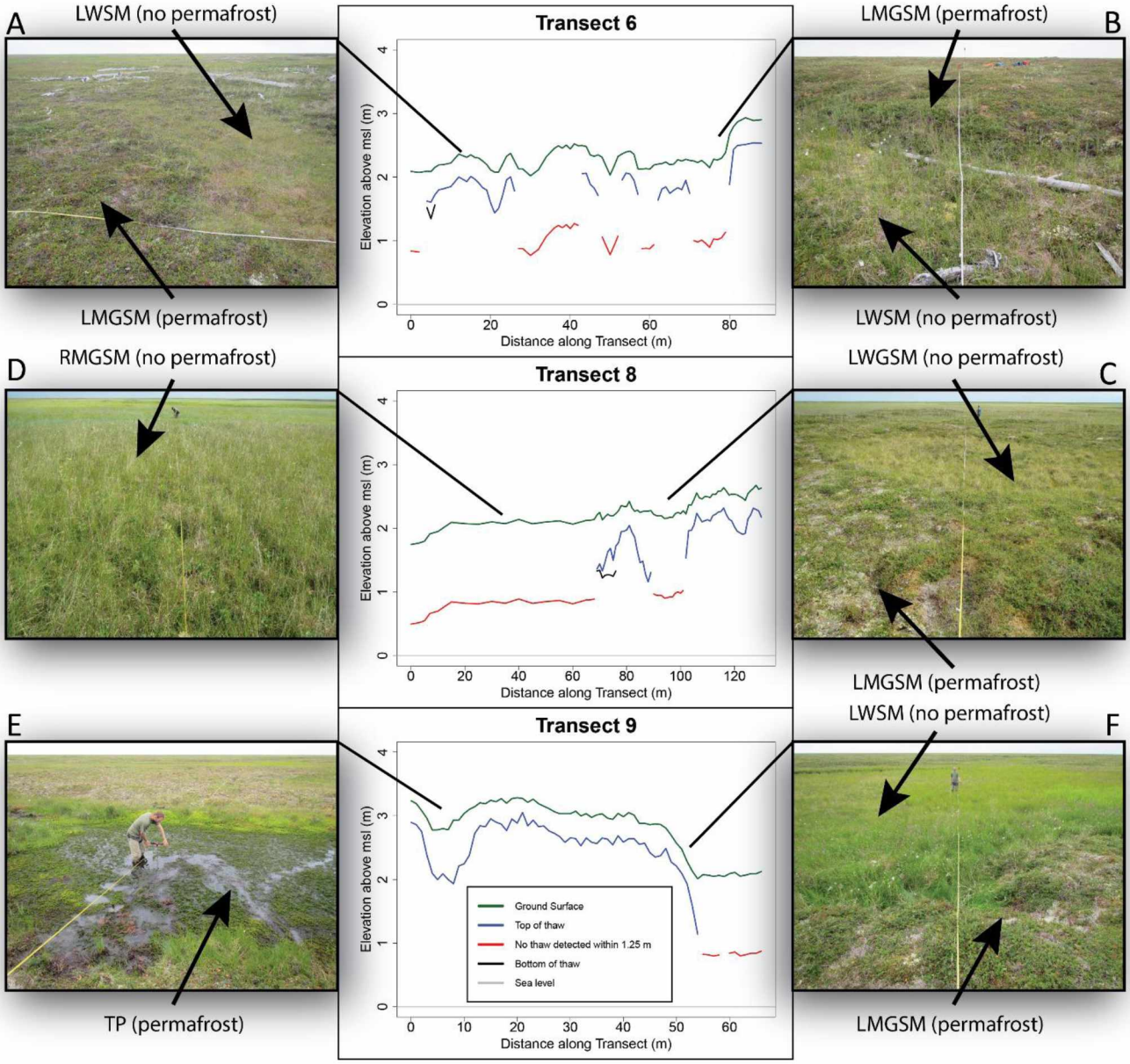

Figure 22. Schematic of Transect 6, Transect, 8, and Transect 9. Transects have thaw depth (blue), thaw bottom (black), no frost (red), and ground surface (green) lines relative to sea level (grey). Key landscape features are annotated with pictures: A) Low permafrost mounds adjacent to plateaus, B) Wrack line on plateau margin, C) Thermo-erosional gully forming (LWGSM), D) RMGSM ecotype after permafrost plateau subsidence, E) Moderately advanced stage Thermokarst Pit, and F) Permafrost plateau margin. Few field probing sites encountered frost thin enough to break through and determine frost thickness. This figure shows two of these areas along the margins of permafrost plateaus in Transect 6 (~5 m along transect) and Transect 8 (~70 m along transect).

4.2 LiDAR Mapping

Results show that the 2.5 (mean + 1 standard deviation) threshold more accurately represents the permafrost landscape when mapping with LiDAR. The 2.30 (mean) cutoff has a higher error of commission (3.0% vs. 0.90%) and identifies levees on the active floodplain as permafrost. Likewise, basins of LMSM around the permafrost plateaus that are above 2.3 m above msl are also mapped as permafrost. Examples of both of these commission errors are designated in Figure 15 with (i) and (ii). Conversely, the map created with the 2.5 threshold omits some permafrost on the inland fringes of the inactive floodplain (Figure 15). This type of error is exemplified by the low-lying permafrost near Transect 7 (Figure 5).

Since this is the type of permafrost that is most vulnerable to disappearing in the near future, an argument could be made to select this more conservative threshold (and increase the error of commission) in order to ensure capturing these instances. Consequently, these small, low-lying permafrost plateaus on the inactive floodplain are also very hard to identify with the spectral data.

Incorporating the probability of near-surface permafrost calculations in mapping the landscape adds another dimension to the analysis. By quantifying the uncertainty of permafrost presence based upon elevation, areas that previously experienced difficulty in mapping permafrost (e.g. Figure 15 (i)) can be examined in the context of the probability of permafrost occurrence (Figure 17 (i)). Not only does the probability mapping add an additional threshold for mapping permafrost, it also describes the morphology of the permafrost in the region. Looking at the probability map, the presence of permafrost is highly probable at higher elevations and the absence of permafrost is highly probable at lower elevations, but the mid-elevations show high uncertainties in permafrost presence. Specifically, these areas of high uncertainty are mostly along the margins of the plateaus, where both elevation and uncertainty fall off abruptly. This abrupt change in probability mirrors the abrupt change in elevation on the landscape. Similarly, the map can also be examined in terms of probability based upon location. An area that shows a relatively high probability of permafrost that is far from the abandoned floodplain will likely not be permafrost in actuality. More likely, the probability in that area is driven by the elevation of a river levee, especially if it is close to a water feature. There is potential to incorporate this type of contextual analysis into the workflow using a weighting system based upon distance to the abandoned floodplain, but it was not explored in this study.

Since the landscape has a general elevation ramp increasing from sea level inland, the specific thresholds used in this study do not apply to the entire YK. In an effort to improve the accuracy of the LiDAR mapping and to remove spurious omission/commission errors, an attempt to remove the overall background elevation ramp of the delta before applying a threshold was explored. This was done by smoothing the LiDAR dataset with a variety of kernel sizes (1,000x1,000 to 10,000x10,000), and subtracting the result from the original LiDAR dataset. While removing the landscape elevation ramp was promising in theory, these efforts, ultimately, did not prove useful, as none of the adjustments improved the map accuracy. Similar to the commission errors identifying levees (Figure 15 (ii)), removing the elevation ramp only increased the identification of relative elevation differences on the delta, accentuating smaller topographical differences across the inland gradient, and not specifically on the abandoned floodplain. This effort added more commission error than improvements at this mapping scale, so it was eventually abandoned. However, this should be taken into consideration when mapping different areas of the delta.

The LiDAR mapping could be improved by incorporating delineations of the landscape into the analysis. For example, errors of commission in areas known not to have permafrost can be reduced by limiting the LiDAR mapping by ecosection or ecodistrict (higher order hierarchical mapping delineations that Jorgenson (2000) defines by geomorphology, soil texture, permafrost, and physiography (Figure 3)). This addition may prove especially useful when mapping over a larger extent, where the correction for elevation ramps in the landscape may be needed. Other datasets may also be useful to incorporate with the LiDAR data in a data fusion approach. For example, high-resolution soil moisture datasets such as NASA's Airborne Microwave Observatory of Subcanopy and Subsurface (AirMOSS) would be useful in providing the distinction between moister permafrost plateaus and drier river levees on the landscape, as well as identifying water features and wet areas on the landscape that should lack permafrost.

4.3 Spectral Mapping

4.3.1 Validation

When discussing the results of the spectral mapping techniques, it is important to note the difference between the accuracy of the model mapping the landscape as a whole, and the

accuracy of the model mapping the permafrost specifically. In general, the spectral workflows mapped the landscape well, but had more trouble accurately mapping the permafrost. This distinction comes from the ratio of the error of omission and the error of commission (permafrost missed or permafrost added), as well as the percentage of the landscape that is covered in permafrost. For example, an error of omission that seems within reason, such as the 7.7% omission from the manual threshold selection of Workflow 2 (Table 12), actually results in 41.8% of the permafrost not being mapped (Table 13), given that the landscape is roughly 19% permafrost (calculated from the LiDAR mapping output). This nuance changes the interpretation of how well the model performs, and is easier to visualize from the error in the output map (Figure 18 or Figure 19). Thus, the percent error of mapping permafrost is especially important to consider when mapping small-scale landscape change and tracking thermokarst processes.

For this reason, it is also important to note the differences in the percentage of the landscape predicted to have permafrost by the validation points, because this changes the calculation of the percent error in mapping permafrost. The four validations conducted in the analysis resulted in four different estimates of permafrost cover (21%, 76%, 24%, and 19%) based on the GPS points used for validation (n=333 and n=62) and the output of the LiDAR mapping on a per pixel basis (n=17,891,000) (Table 15). The GPS points within the AOI (n=62) erroneously assume 75.58% of the landscape is permafrost, which is likely a function of how few points there were, and a bias towards sampling more permafrost while on the plateaus. This bias may also have been a function of how much land is on the abandoned floodplain, and the inability to collect points in water bodies. Considering these biases, the limited GPS points collected in the field do not necessarily produce an accurate representation of how much permafrost is actually on the landscape within the mapping AOI. The other three estimates agree that the permafrost cover is somewhere between 18% and 24%, which puts this landscape on the lower end of the sporadic permafrost classification.

Table 15. Percent of the landscape predicted to have permafrost, as calculated from the various validation sets. The LiDAR map was validated using 333 GPS points, of which 71 (21.3%) were permafrost. The spectral maps were validated using both GPS points, and the resultant map of the LiDAR mapping. The validation with GPS used 62 points, of which 45 (75.6%) were permafrost. The validation using the LiDAR output used the entire AOI (17,892,000 pixels) and found 23.7% and 18.5% permafrost cover with the 2.3 m above msl (mean) and the 2.5 m above msl (mean + 1 standard deviation) thresholds, respectively.

	LiDAR	**Spectral**		
			LiDAR Output	
	GPS	GPS	2.3 m above msl Threshold	2.5 m above msl Threshold
# Total validation points (pixels)	333	62	(17,892,000)	(17,892,000)
# Permafrost points (pixels)	71	45	(4,246,157)	(3,315,876)
Percent permafrost cover	**21.3%**	**75.6%**	**23.7%**	**18.5%**

The notable lack of validation in the AOI was also due in part to logistical difficulties in the field, as the channel of the Tutakoke river narrowed and became shallower closer to the abandoned floodplain, restricting access to the eastern portion of the AOI by boat. This lack of GPS data led to the adoption of the LiDAR output map as a means to validate the spectral mapping.

The main advantage of using the LiDAR to validate the spectral mapping was the ability to validate on a per pixel basis. This increased the validation from 62 points to over 17,000,000 pixels. This method is a little unorthodox because it introduced error into the validation, but was used anyway because of the high mapping accuracy the LiDAR produced (94.9%) and the lack of GPS validation points within the AOI. To remove bias in future sampling and avoid error propagation issues, validation points should be collected in a more systematic manner, and include more points within the AOI.

This also raises the question of how accurate the validation for the spectral mapping using GPS points really was, as accuracies were lower across the board compared to the validation using the LiDAR output map. As an example, consider the manual Workflow 1 validation. Also, note that the validation of the spectral techniques with the LiDAR output map is not a metric of how well the spectral mapping performed, but rather a metric of how well it agreed with the LiDAR output map. With this in mind, it is peculiar that the spectral mapping agrees well with the LiDAR mapping (89.4%, n=~17,000,000) that had a high validation (94.9%,

n=333), but has relatively low validation values when validated with the GPS (62.9%, n=62). Furthermore, when calculating the probability that the spectral mapping was correct given it agreed with the LiDAR and the LiDAR was correct (Equation 3), the probability (0.61, n=57) was on the same order of magnitude that the original validation using GPS points was on (i.e. ~60% accuracy). This consistency may in fact be attributable to the low number of validation points again, because the probability calculation relies on validation points that are concurrent between the two datasets. Higher validation from the LiDAR may also be explained by the higher proportion of pixels that are on the healthy centers of plateaus compared to the GPS points that sampled more of the margins of the plateaus. This nuance may suggest that the spectral techniques better identify vegetation in the center of the plateaus (i.e. lichen and moss) than vegetation on the margins (i.e. shrubs).

4.3.2 Ad-hoc Masking Technique

An additional source of error may come from the ad-hoc masking technique itself: specifically, masking out the shallow thermokarst pits on the plateaus. Even though these pits are an indication that the plateaus are degrading, field observations found that permafrost is still present beneath these ponds. This means that permafrost is present under the smaller bodies of water on the plateaus. By masking out all of the water features detected from the PCA, some of the pits on the plateaus (underlain by permafrost) were masked out of the final analysis. In an effort to quantify this error, the areas identified as permafrost from the LiDAR DEM were used to extract values from the complete mask applied in the spectral analysis. This served to validate the mask layer based upon the LiDAR output map. Results showed 98.9% of the plateaus were not masked out by the masks, with only 1.1% masked in error. This low error shows that the mask worked well in identifying and removing areas that were not permafrost.

Additional error of omission may have come from error associated with thaw probing in the field. If seasonal frost was misidentified as permafrost in the field, that error would in turn be carried through to the validation, skewing the results. This potential error is ultimately a result of the timing of our fieldwork.

The ad-hoc masking technique also originally included a mask for the driftwood, as it was an assumed region of degrading permafrost. However, upon discovery during fieldwork that the permafrost was relatively stable under drift lines, the wood mask was not included in the

final workflow with the water and shoreline masks. Created using the base of Workflow 1, the driftwood mask took the statistical variance of a 5x5 kernel, to identify drift lines in the scene, then used a watershed thresholding to isolate the drift lines. This technique worked on the scene mainly because the driftwood is bright across the visible spectrum, and multiplying the three bands together exaggerated the reflectance of the wood in comparison to other features in the scene. The brightest responses in the blue band are generally driftwood, so applying a strict threshold with a high cutoff is also a viable option, but needs further exploration. Though not directly applicable to this study, the automated driftwood mapping has pronounced potential for reconstructing storm surge inundation and flood extent mapping (Figure 23) (Terenzi et al. 2014).

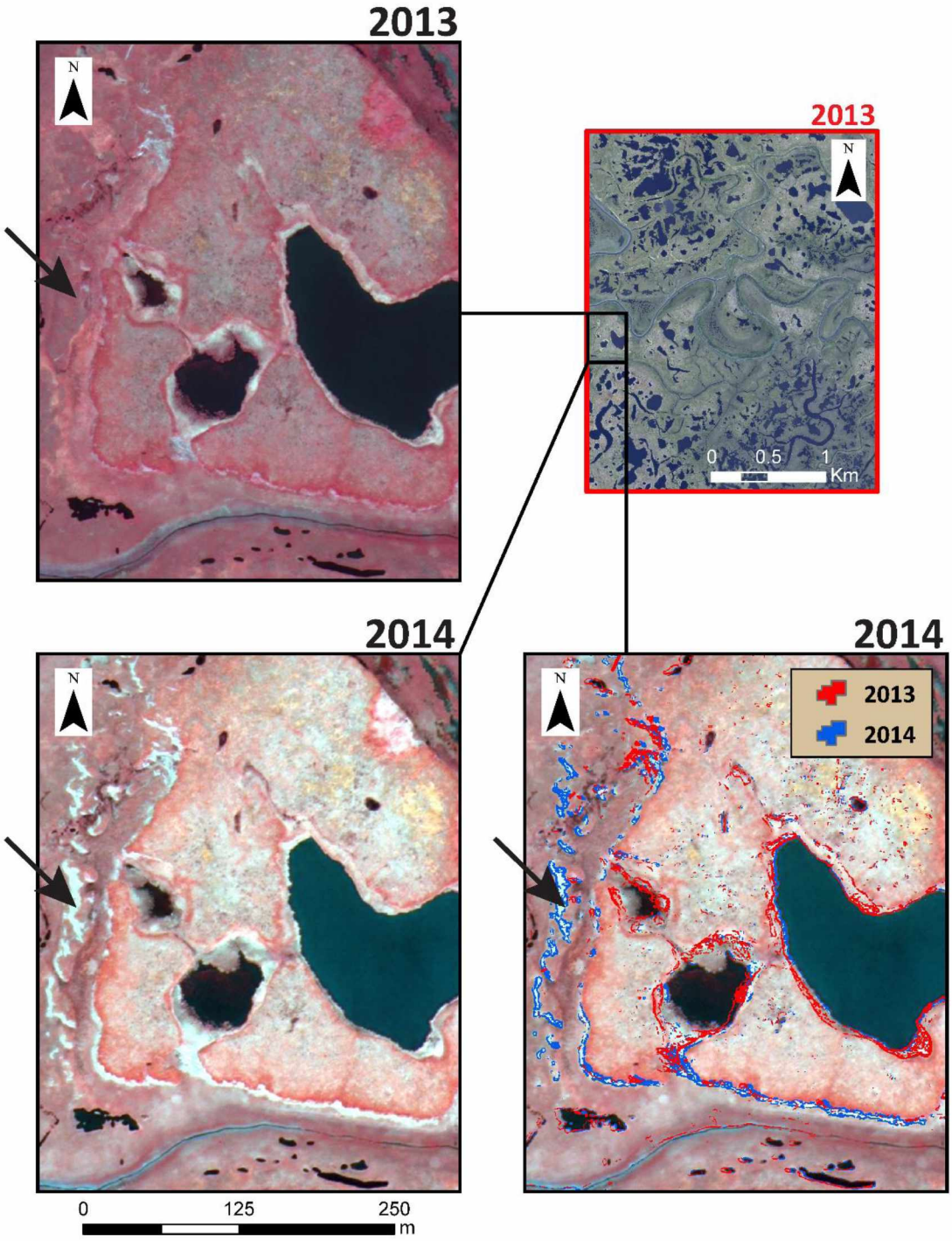

Figure 23. Example of driftwood detection mask, with potential applications for storm surge reconstruction. The 2013 WorldView 02 scene shows the AOI extent in a true-color R-G-B (5-3-2) band combination, and the insets show the 2013 and 2014 WorldView 02 scenes in a false color infrared NIR-Y-G (8-4-3) band combination. Arrows in the insets show differences in driftwood distribution between 2013 and 2014. Satellite imagery © 2017 Digital Globe, NextView license.

4.3.3 Spatial and Temporal Landscape Heterogeneity

In a physical context, the permafrost proved difficult to map using spectral techniques because of the heterogeneity of the vegetation on the plateaus. In general, shrubbier vegetation such as *Betula nana* and *Empetrum nigrum* tend to grow in denser patches on the margins of the plateaus, with more lichen and moss growth towards the center. Spectrally, this appears as brighter NIR returns around the edges of the plateaus, and generally lower NIR returns towards the center. This creates a doughnut-like shape, which is harder to identify than a uniform plateau. Furthermore, differences in lichen species-composition create a range of spectral returns from dark (e.g. *Bryocaulins divergens*) to light (e.g. *Cladina rangiferina*). This variation creates a speckled spectral return, which was why texture analysis and smoothing proved useful. Differences in moisture and water distribution due to micro-topographical depressions on the plateaus, such as thermokarst pits and initial degradation, also contribute to the mixed spectral return. This heterogeneous nature of the plateaus can be seen easily in Figure 23.

To reduce this heterogeneity, speckle reduction techniques, such as the low-pass filter applied in this analysis are needed. A useful strategy for future mapping efforts may be to employ a multiscale-driven approach to optimize the level of smoothing before threshold selection, similar to what Ajadi et al. (2016) employ with Synthetic Aperture Radar (SAR) over fire scars south of Fairbanks, AK. The need for this reduction in spatial resolution attests to the fact that high resolution images do not necessarily lead to high accuracies in mapping the landscape, as sometimes lower resolution data is better suited to mapping. This is true in the case of the spectral workflow, as the heterogeneity of the plateaus caused speckle in the high resolution images. Introducing high-resolution soil moisture products (e.g. AirMOSS) would potentially be useful in adjusting the radiance values of the scene based upon soil moisture, to help identify areas with consistent soil moisture as potential sites for permafrost.

Overall, the main problem with the spectral mapping workflows was that the algorithm outlined in this thesis was more or less optimized for the 2007 scene, and did not replicate well across time. The temporal failure of the algorithm largely comes from the differing conditions during the image acquisition. Specifically, differences in phenology and landscape hydrology drove the spectral differences between scenes. Similarly, scenes varied based upon the type and spectral resolution of the sensor. The earlier datasets (e.g. IKONOS, QuickBird02) only had visible and NIR bands associated with them, and the 1988 flight only had color infrared data. In

contrast, the later WorldView 02 scenes had eight spectral bands, making the analysis (especially the PCA) stronger and more robust. Failure of the processing workflows to adjust to these conditions led to problems extrapolating the algorithms across scenes. This can be seen from the percent of the landscape mapped as permafrost and the percent error in mapping permafrost over time (Figure 20 and Figure 21). While Workflow 2 replicated across scenes better than Workflow 1, neither performed well enough to discern small scale changes in permafrost that is indicative of the degradation in the region.

4.4 Viability

4.4.1 LiDAR Mapping

Though LiDAR data is used fairly frequently in permafrost degradation studies, it is rarely used in mapping permafrost distribution explicitly. As of now, no mapping effort using solely LiDAR data has been published. This analysis shows that, given the right permafrost conditions and landscape characteristics, LiDAR can be used to map permafrost extent with great precision. Most of this success comes from the unique landscape of the YKD and the strong correlation between permafrost and elevation. Nonetheless, in this context LiDAR is the most accurate mapping method tested in this study, and has proved a valuable tool for mapping. Future LiDAR collections over the area will greatly enhance the understanding of permafrost in the region.

Using LiDAR to map permafrost extents also has the potential to be expanded to other study areas. Relatively flat landscapes with permafrost containing massive ice or, as shown in this study, segregated ice can be mapped using elevation as a proxy for ice accretion and thus permafrost presence. Current possibilities include collapse-scar bogs or similar landscapes, as well as other areas with permafrost on relatively flat terrain. This method is particularly useful in regions with sporadic to isolated permafrost, and its utility decreases with increasing permafrost cover. As the Arctic warms, LiDAR may become useful over other arctic deltas that currently have temperatures indicative of climate-driven permafrost but will likely look more like the YKD with ecosystem-driven or ecosystem-protected conditions in the future (Shur and Jorgenson 2007).

However, there are limitations to using LiDAR to map permafrost extensively. First and foremost is the cost of LiDAR acquisition and processing. Current rates for LiDAR flights are expensive, even assuming a fairly large area covered with lower point density. Secondly, processing time for DEM creation and geolocation are costly, both in time and data storage. These drawbacks are both a function of the scale of mapping, which is an important consideration when using LiDAR. The relatively small spatial scale of this analysis lends itself well to LiDAR, but expanding the scope to a regional scale is, unfortunately, unrealistic at present. However, current and planned LiDAR flights will soon expand landscape coverage in the region by ten times or more (USGS-3DEP 2015, Murphy 2016).

Other datasets, such as high resolution IfSAR (Interferometric-SAR) or space-borne laser altimeter systems still have resolutions that are too spatially and vertically coarse (on the order of several meters) to provide adequate mapping data for the permafrost plateaus. However, a technology that does have merit is high resolution Structure-from-Motion (SfM) processing. Since SfM relies on spectral datasets, collection costs are minimal compared to LiDAR campaigns. The fact that SfM processing only creates a digital surface model as opposed to a digital elevation model (roughly equivalent to the first return of a LiDAR collect, rather than the last return) is mitigated by the minimal structure of the vegetation canopy on the delta. In other areas where shrub or tree cover demand elevation rather than surface models, SfM becomes a poor substitute for LiDAR, but on the flat low-growing tundra of the delta, the SfM technique has potential. The SfM derived surface models from the recently released Arctic-DEM still do not have the vertical resolution needed to map permafrost plateaus, which may be because the Arctic-DEM creates a composite model from many scenes (Polar Geospatial Center 2017). However, SfM or stereo-processing of a single image pair could result in better vertical resolution, which warrants further research.

Repeat pass LiDAR over the areas that have already been collected introduces another level of analysis. One advantage of LiDAR is the ability for 3-dimensional analysis. With repeat pass LiDAR over the permafrost plateaus, a volumetric analysis of landscape change is possible, which has a myriad of applications. Tracking of thermokarst pit development, subsidence of plateaus, potential carbon emissions from permafrost thaw, and redistribution of driftwood are a few of the possibilities repeat pass LiDAR offers in addition to tracking lateral movement of the permafrost plateau margins. Currently, there is increased interest in flying LiDAR in the region,

especially along the coast. Weather permitting, NASA is also planning a LiDAR acquisition over the study site in Summer 2017.

4.4.2 Spectral Mapping

The mixed results of the spectral mapping analysis performed here raise doubts about the viability of using spectral datasets alone as a useful technique for mapping permafrost. While model validation for the 2007 IKONOS scene demonstrated that using only spectral means to map permafrost can be done with moderate success, the lack of continuity across time and sensors hobbles the ability to track thermokarst and permafrost degradation. For imagery with similar spectral properties as the 2007 IKONOS scene, permafrost mapping across times may have potential. The automated processing workflow was successful to an extent, but a more robust metric for threshold selection is needed to make the workflow(s) completely unsupervised and still successful. However, if a stable algorithm can be established, the ability to map permafrost over large swaths of the YKD would not be unreasonable given the extent and availability of high-resolution satellite remote sensing data. A Bayesian approach to optimizing the threshold selection could vastly improve this process.

Unfortunately, lower resolution imagery would not be sufficient in resolving the plateaus in the region. Even moderate resolution imagery such as Landsat (30 m resolution) would still be too coarse to distinguish between plateaus with meaningful results. Since the aim of this study is to create a baseline dataset for monitoring change in the plateaus, a resolution that is fine enough to register change must be used for mapping. The plateaus in the region are experiencing thermokarst rates <1 m/year, so high spatial resolution is needed in order to track changes over time.

In terms of affordability, the spectral mapping would be significantly cheaper than the LiDAR mapping, even if imagery needed to be purchased from Digital Globe, Inc. The high resolution of increasingly available products allows for smaller scale mapping across large swaths of land. Because of these advantages, pursuing a spectral – or at least partially spectral – method to mapping permafrost is attractive, and should be considered.

Despite the shortcomings of the spectral mapping algorithm, useful information has come from the analysis, and individual components of the workflows will definitely prove useful in subsequent analyses. For example, the techniques used to mask water and wood have potential

for landscape scale analyses of hydrological changes and storm surge reconstructions, respectively. Similarly, the identification of what is not permafrost is also useful in its own sense, as it provides a deeper understanding of the thermal regime in the region. The relatively high accuracy of mapping the landscape as a whole (as opposed to mapping the permafrost specifically) provides further insights into the type of permafrost cover present on the YKD and the role permafrost plays on the landscape.

Overall, better methods of calculating thermokarst rates on the landscape exist, which are more useful than the spectral workflows explored here. Specifically, manual delineation of the permafrost boundaries and subsequent processing using the United States Geological Survey (USGS) Digital Shoreline Analysis System (DSAS) provide a much more accurate estimate of thermokarst rates. A downside to this processing technique is the time-intensive manual delineations of the plateau edges, so this analysis is restricted to smaller scales. Overall, though, the rates calculated will provide better insight than anything calculated from these spectral workflows.

4.5 Broader Impacts

This research, though implemented at a small scale, has both regional and global implications. As the Arctic warms, the stability of the permafrost on the YKD is vulnerable to rising air temperatures. At the same time, projected increases in storm frequency and intensity coupled with the increased uncertainty in sea ice concentrations and snow cover will likely result in more storms with larger storm surges. This duality in disturbance mechanisms is mirrored by the duality in thermokarst processes. The press mechanism of rising air temperatures manifests as thermokarst pits on top of the plateaus, while the pulse mechanism of periodic storm surges manifests as lateral degradation of the plateaus. In this way, geomorphic indicators on the plateaus reflect the larger scale change occurring around the Arctic. Mapping permafrost extent in high resolution is important to tracking these permafrost degradation processes, and is important for community planning and land management.

As the YKD supports many Alaska Natives, any change on the landscape will have repercussions throughout the local subsistence communities. The permafrost plateaus are a major landscape feature that provide important services to the Yup'ik and Cup'ik people. For

instance, berries such as *Rubus chamaemorus* (cloudberry) and *Empetrum nigrum* (crowberry) are concentrated on the plateaus, which are a staple in the native diet. In the case of *Rubus chamaemorus*, the permafrost plateaus are the only habitat on the delta, which has major implications for future subsistence gathering. Similarly, much of the cultural heritage of the native communities is on the permafrost plateaus. Burial sites, sod houses, and ancient villages were originally built on the plateaus because of the drier and higher ground. Now, local communities are observing subsidence and disappearance of important pieces of their heritage. The ancient village of Englullugpagmiut is just one of many examples that has shown subsidence in recent years.

The permafrost plateaus also play an important role in the life cycle of many animal species. One species that will be directly impacted by degrading permafrost is the *Numenius tahitiensis* (Bristle-thighed curlew), which has a limited geographic range and is already a species of conservation concern. This Whimbrel-like bird breeds further inland on parts of the Seward Peninsula and the Nulato Hills region, and the entire global population uses the permafrost plateaus on the YKD as a staging ground for its trans-pacific migration. The berries on the permafrost provide crucial nutrients for a transoceanic migration that can exceed 6,000 km in length (Marks et al. 2002).

In terms of the YKD as a whole, the degradation of the permafrost is just one aspect of the changing landscape. Increases in shrub cover and changes in vegetation communities will continue even after the permafrost is gone. However, because of the susceptibility of the permafrost to thermal disturbance, the permafrost plateaus are the vanguard of landscape change in the region. Degradation of these plateaus will have lasting impacts on the communities that rely on them. Studying thermokarst processes and rates of change is an important undertaking, as results will likely impact community resource planning. The permafrost in the region will certainly be gone by the end of the century, but likely much sooner (Jorgenson and Ely 2001, Pastick et al. 2015). Given this short timeline, local communities will need to adapt quickly in order to preserve their culture and way of life.

5. CONCLUSION

This analysis explored two novel approaches to mapping permafrost distribution on the YKD of Alaska. Both methods were fairly unconventional in that they relied solely on a single type of remote sensing data, using field measurements taken in July 2016 as validation. The first method, which utilized a 2009 LiDAR dataset, was very successful in mapping permafrost extent based upon elevation boundaries of the LMGSM ecotype observed in the field. This method resulted in 95.21% accuracy in mapping the landscape, with a relatively low error of omission (4.79%). The second method explored contrasting workflows analyzing high resolution aerial and satellite imagery in an automated and semi-automated fashion for each workflow. Accuracies in mapping the landscape varied from 78.14% (automated threshold selection of Workflow 1) to 89.40% (manual threshold selection of Workflow 1). Though apparently successful, the spectral mapping techniques' percent error in mapping permafrost was still ~41% for the manual threshold selections, and as high as 59.72% for the automated threshold selection in Workflow 2. Moreover, the spectral mapping technique developed for the 2007 scene did not replicate well across time, which was most likely a product of seasonal differences in the scenes. Thus, neither spectral mapping workflow explored in this thesis performed well enough over multiple time periods to identify the small-scale changes occurring on the landscape.

The LiDAR workflow is viable for mapping permafrost in the region, and has implications for detecting small-scale changes in the morphology of the plateaus through time with repeat coverage. Conversely, the spectral analysis did not perform well enough for consideration in long-term thermokarst monitoring or landscape change detection. However, the maps created from the spectral workflows (at least for the 2007 scene) do have merit, as they address local scale permafrost extent in an under-mapped region, and they have the potential to be easily expanded. Overall, this analysis demonstrates the viability of applying LiDAR and spectral datasets to mapping permafrost distribution on the YKD, where otherwise conventional permafrost mapping techniques would not be viable. Conclusions from this study will hopefully inform the permafrost mapping community about the viability of LiDAR for mapping permafrost in some contexts, as well as useful image processing techniques pertinent to mapping permafrost at any scale.

Techniques explored in this thesis are a first step to the automatic creation of permafrost maps in the region. These baseline maps are essential reference datasets for monitoring

thermokarst and future change. Understanding the thermokarst processes and permafrost resilience at the larger regional scale gives insight into how the YKD will change as a region, as well as other Arctic deltas in the future. The timeline over which these plateaus degrade will directly impact native communities within the next generation, and are thus an important feature to monitor.

6. LITERATURE CITED

Ager, T. A. 1982. Vegetational history of western Alaska during the Wisconsin glacial interval and the Holocene. *Paleoecology of Beringia. Academic Press, New York*, 75-93.

Airborne Imaging. 2011. Final LiDAR Processing & Vertical Accuracy Report: Prepared for the U.S. Fish and Wildlife Service *LiDAR Imagery & DEM Model for Yukon Delta National Wildlife Refuge - Near Angyaravak Bay, Alaska* (pp. 28). Calgary, Alberta, Canada: Airborne Imaging.

Ajadi, O. A., Meyer, F. J., & Webley, P. W. 2016. Change Detection in Synthetic Aperture Radar Images Using a Multiscale-Driven Approach. *Remote Sensing, 8*(6), 482.

Beck, I., Ludwig, R., Bernier, M., Lévesque, E., & Boike, J. 2015. Assessing Permafrost Degradation and Land Cover Changes (1986–2009) using Remote Sensing Data over Umiujaq, Sub-Arctic Québec. *Permafrost and Periglacial Processes, 26*(2), 129-141.

Brown, J., Ferrians Jr, O., Heginbottom, J., & Melnikov, E. 1997. *Circum-Arctic map of permafrost and ground-ice conditions*.

Cuff, D., & Goudie, A. 2009. *The Oxford companion to global change*: Oxford University Press.

Duk-Rodkin, A., Barendregt, R., White, J., & Singhroy, V. 2001. Geologic evolution of the Yukon River: implications for placer gold. *Quaternary International, 82*(1), 5-31.

Dunnett, C. W. 1980. Pairwise multiple comparisons in the homogeneous variance, unequal sample size case. *Journal of the American Statistical Association, 75*(372), 789-795.

ENVI. 2015. Boulder, Colorado: Exelis Visual Information Solutions.

ESRI. 2015. ArcGIS Desktop: Release 10.4. Redlands, CA: Enivronmental Systems Research Institute.

Fienup-Riordan, A., & Rearden, A. 2013. *Ellavut/Our Yup'ik World and Weather: Continuity and Change on the Bering Sea Coast*: University of Washington Press.

Fleming, K., Johnston, P., Zwartz, D., Yokoyama, Y., Lambeck, K., & Chappell, J. 1998. Refining the eustatic sea-level curve since the Last Glacial Maximum using far-and intermediate-field sites. *Earth and Planetary Science Letters, 163*(1), 327-342.

Fleming, K. M. 2000. *Glacial rebound and sea-level change: constraints on the Greenland ice sheet*: Australian National University.

GDAL. 2015. GDAL - Geospatial Data Abstraction Library, Version 2.1.0 (2.1.0 ed.): Open Source Geospatial Foundation.

Gogineni, P., Romanovsky, V., Cherry, J., Duguay, C., Goetz, S., Jorgenson, M., & Moghaddami, M. 2014. Opportunities to use Remote Sensing in Understanding

Permafrost and Related Ecological Characteristics: Report of a Workshop, 97 pp. *Natl. Acad. of Sci., Washington, DC*.

Haralick, R. M., & Shanmugam, K. 1973. Textural features for image classification. *IEEE Transactions on systems, man, and cybernetics, 3*(6), 610-621.

Heginbottom, J. A. 2002. Permafrost mapping: a review. *Progress in Physical Geography, 26*(4), 623-642.

Hinzman, L. D., Bettez, N. D., Bolton, W. R., Chapin, F. S., Dyurgerov, M. B., Fastie, C. L., Griffith, B., Hollister, R. D., Hope, A., & Huntington, H. P. 2005. Evidence and implications of recent climate change in northern Alaska and other arctic regions. *Climatic Change, 72*(3), 251-298.

Jafarov, E. E., Marchenko, S. S., & Romanovsky, V. 2012. Numerical modeling of permafrost dynamics in Alaska using a high spatial resolution dataset. *The Cryosphere, 6*(3), 613-624.

Jolliffe, I. 2002. *Principal component analysis*: Wiley Online Library.

Jones, B. M., Grosse, G., Arp, C. D., Miller, E., Liu, L., Hayes, D. J., & Larsen, C. F. 2015. Recent Arctic tundra fire initiates widespread thermokarst development. *Scientific reports, 5*.

Jones, B. M., Stoker, J. M., Gibbs, A. E., Grosse, G., Romanovsky, V. E., Douglas, T. A., Kinsman, N. E., & Richmond, B. M. 2013. Quantifying landscape change in an arctic coastal lowland using repeat airborne LiDAR. *Environmental Research Letters, 8*(4), 045025.

Jones, E., Oliphant, T., Peterson, P., & Others. 2001-. SciPy: Open source scientific tools for Python, Version 0.17.0-1.

Jorgenson, M. T. 2000. Hierarchical organization of ecosystems at multiple spatial scales on the Yukon-Kuskokwim Delta, Alaska, USA. *Arctic, Antarctic, and Alpine Research*, 221-239.

Jorgenson, M. T., & Grosse, G. 2016. Remote Sensing of Landscape Change in Permafrost Regions. *Permafrost and Periglacial Processes, 27*(4), 324-338.

Jorgenson, M. T., Romanovsky, V., Harden, J., Shur, Y., O'Donnell, J., Schuur, E. A., Kanevskiy, M., & Marchenko, S. 2010. Resilience and vulnerability of permafrost to climate change This article is one of a selection of papers from The Dynamics of Change in Alaska's Boreal Forests: Resilience and Vulnerability in Response to Climate Warming. *Canadian Journal of Forest Research, 40*(7), 1219-1236.

Jorgenson, M. T., & Roth, J. E. 2010. *Landscape Classification and Mapping for the Yukon-Kuskokwim Delta, Alaska*. Fairbanks AK: ABR, Inc.-Environmental Research & Service.

Jorgenson, M. T., Yoshikawa, K., Kanevskiy, M., Shur, Y., Romanovsky, V., Marchenko, S., Grosse, G., Brown, J., & Jones, B. 2008. *Permafrost characteristics of Alaska.* Paper presented at the Proceedings of the Ninth International Conference on Permafrost.

Jorgenson, T., & Ely, C. 2001. Topography and flooding of coastal ecosystems on the Yukon-Kuskokwim Delta, Alaska: implications for sea-level rise. *Journal of Coastal Research*, 124-136.

Klein, D. R. 1966. Waterfowl in the economy of the Eskimos on the Yukon-Kuskokwim Delta, Alaska. *Arctic*, 319-336.

Kokelj, S., & Jorgenson, M. 2013. Advances in thermokarst research. *Permafrost and Periglacial Processes, 24*(2), 108-119.

Lantz, T. C., Marsh, P., & Kokelj, S. V. 2013. Recent shrub proliferation in the Mackenzie Delta uplands and microclimatic implications. *Ecosystems, 16*(1), 47-59.

Liljedahl, A. K., Boike, J., Daanen, R. P., Fedorov, A. N., Frost, G. V., Grosse, G., Hinzman, L. D., Iijma, Y., Jorgenson, J. C., & Matveyeva, N. 2016. Pan-Arctic ice-wedge degradation in warming permafrost and its influence on tundra hydrology. *Nature Geoscience*.

Lin, D., Johnson, D., Andresen, C., & Tweedie, C. 2012. High spatial resolution decade-time scale land cover change at multiple locations in the Beringian Arctic (1948–2000s). *Environmental Research Letters, 7*(2), 025502.

Marchenko, S., Romanovsky, V., & Tipenko, G. 2008. *Numerical modeling of spatial permafrost dynamics in Alaska.* Paper presented at the Proceedings of the Ninth International Conference on Permafrost.

Marks, J., Tibbitts, T., Gill, R., & McCaffery, B. 2002. Bristle-thighed curlew (Numenius tahitiensis). *Birds of North America, 705*, 1-36.

Milne, G. A., Long, A. J., & Bassett, S. E. 2005. Modelling Holocene relative sea-level observations from the Caribbean and South America. *Quaternary Science Reviews, 24*(10), 1183-1202.

Minsley, B. J., Abraham, J. D., Smith, B. D., Cannia, J. C., Voss, C. I., Jorgenson, M. T., Walvoord, M. A., Wylie, B. K., Anderson, L., & Ball, L. B. 2012. Airborne electromagnetic imaging of discontinuous permafrost. *Geophysical Research Letters, 39*(2).

Murphy, K. (Cartographer). 2016. Agency Priorities fro 3DEP LiDAR Collection - Yukon-Kuskokwim Delta

Naito, A. T., & Cairns, D. M. 2015. Patterns of shrub expansion in Alaskan arctic river corridors suggest phase transition. *Ecology and evolution, 5*(1), 87.

NOAA/NCDC. 2017. Daily temperature record for Bethel Airport, AK US 1923-2016; GHCND:USW00026615. National Oceanic and Atmospheric Administration (NOAA).

Otsu, N. 1979. An automatic threshold selection method based on discriminate and least squares criteria. *Denshi Tsushin Gakkai Ronbunshi, 63*, 349-356.

Paine, J. G., Andrews, J. R., Saylam, K., Tremblay, T. A., Averett, A. R., Caudle, T. L., Meyer, T., & Young, M. H. 2013. Airborne lidar on the Alaskan North Slope: Wetlands mapping, lake volumes, and permafrost features. *The Leading Edge, 32*(7), 798-805.

Panda, S., Prakash, A., Jorgenson, M., & Solie, D. 2012. Near-surface permafrost distribution mapping using logistic regression and remote sensing in Interior Alaska. *GIScience & Remote Sensing, 49*(3), 346-363.

Panda, S. K., Prakash, A., Solie, D. N., Romanovsky, V. E., & Jorgenson, M. T. 2010. Remote sensing and field-based mapping of permafrost distribution along the Alaska Highway corridor, interior Alaska. *Permafrost and Periglacial Processes, 21*(3), 271-281.

Pastick, N. J., Jorgenson, M. T., Wylie, B. K., Minsley, B. J., Ji, L., Walvoord, M. A., Smith, B. D., Abraham, J. D., & Rose, J. R. 2013. Extending airborne electromagnetic surveys for regional active layer and permafrost mapping with remote sensing and ancillary data, Yukon Flats Ecoregion, Central Alaska. *Permafrost and Periglacial Processes, 24*(3), 184-199.

Pastick, N. J., Jorgenson, M. T., Wylie, B. K., Nield, S. J., Johnson, K. D., & Finley, A. O. 2015. Distribution of near-surface permafrost in Alaska: Estimates of present and future conditions. *Remote Sensing of Environment, 168*, 301-315.

Péwé, R., & Brown, T. 1973. *Distribution of permafrost in North America and its relationship to the environment: a review, 1963-1973.* Paper presented at the Permafrost: North American Contribution [to The] Second International Conference.

Polar Geospatial Center. 2017. *Arctic DEM.* Retrieved from: http://www.pgc.umn.edu/arcticdem

R Development Core Team. 2016. R: A language and environment for statistical computing. Vienna, Austria: R Foundation for Statistical Computing. Retrieved from www.R-project.org

Raynolds, M. K., Walker, D. A., Ambrosius, K. J., Brown, J., Everett, K. R., Kanevskiy, M., Kofinas, G. P., Romanovsky, V. E., Shur, Y., & Webber, P. J. 2014. Cumulative geoecological effects of 62 years of infrastructure and climate change in ice-rich permafrost landscapes, Prudhoe Bay Oilfield, Alaska. *Global change biology, 20*(4), 1211-1224.

Riseborough, D., Shiklomanov, N., Etzelmüller, B., Gruber, S., & Marchenko, S. 2008. Recent advances in permafrost modelling. *Permafrost and Periglacial Processes, 19*(2), 137-156.

Romanovsky, V. E., Smith, S. L., & Christiansen, H. H. 2010. Permafrost thermal state in the polar Northern Hemisphere during the international polar year 2007–2009: a synthesis. *Permafrost and Periglacial Processes, 21*(2), 106-116.

Schuur, E., McGuire, A., Schädel, C., Grosse, G., Harden, J., Hayes, D., Hugelius, G., Koven, C., Kuhry, P., & Lawrence, D. 2015. Climate change and the permafrost carbon feedback. *Nature, 520*(7546), 171-179.

Shur, Y., & Jorgenson, M. 2007. Patterns of permafrost formation and degradation in relation to climate and ecosystems. *Permafrost and Periglacial Processes, 18*(1), 7-19.

Slater, A. G., & Lawrence, D. M. 2013. Diagnosing present and future permafrost from climate models. *Journal of Climate, 26*(15), 5608-5623.

Soille, P. 2013. *Morphological image analysis: principles and applications*: Springer Science & Business Media.

Swanson, D. 2013a. Permafrost landforms as indicators of climate change in the Arctic Network of National Parks. *Alaska Park Science, 12*, 40-45.

Swanson, D. 2013b. Three Decades of Landscape Change in Alaska's Arctic National Parks: Analysis of Aerial Photographs, c. 1980–2010. *NP Service, Ed., Fort Collins*.

Terenzi, J., Jorgenson, M. T., Ely, C. R., & Giguère, N. 2014. Storm-surge flooding on the Yukon-Kuskokwim Delta, Alaska. *Arctic*, 360-374.

Thorsteinson, L. K., Becker, P. R., & Hale, D. A. 1989. *The Yukon Delta: A Synthesis of Information*. Anchorage, AK: OCS Study, MMs 89-0081.

Tremblay, B., Lévesque, E., & Boudreau, S. 2012. Recent expansion of erect shrubs in the Low Arctic: evidence from Eastern Nunavik. *Environmental Research Letters, 7*(3), 035501.

Tyrtikov, A. P. 1964. Perennially frozen ground and vegetation (R. J. E. Brown, Trans.) *Principles of geocryology (permafrost studies), Part I, General geocryology, Chapter XII*. Moscow: Academy of Sciences of the U.S.S.R.

USGS-3DEP. 2015. *U.S. Geological Survey Broad Agency Announcement for 3D Elevation Program (3DEP) G15PS00558*. USGS.

Walt, S. v. d., Schönberger, J. L., Nunez-Iglesias, J., Boulogne, F., Warner, J. D., Yager, N., Gouillart, E., Yu, T., & contributors., s.-i. 2014. scikit-image: Image processing in Python (Vol. 2:e453). PeerJ.

Westermann, S., Østby, T., Gisnås, K., Schuler, T., & Etzelmüller, B. 2015. A ground temperature map of the North Atlantic permafrost region based on remote sensing and reanalysis data. *The Cryosphere, 9*(3), 1303-1319.

Zhang, Y., Chen, W., & Riseborough, D. W. 2008. Disequilibrium response of permafrost thaw to climate warming in Canada over 1850–2100. *Geophysical Research Letters, 35*(2).

Zhang, Y., Olthof, I., Fraser, R., & Wolfe, S. A. 2014. A new approach to mapping permafrost and change incorporating uncertainties in ground conditions and climate projections. *The Cryosphere, 8*(6), 2177-2194.